ВЫПУСКНАЯ КВАЛИФИКАЦИОННАЯ РАБОТА
GRADUATION THESIS

Моделирование фотолюминесценции в плазмонных метаповерхностях на основе нановыпуклостей / Simulation of Photoluminescence in Plasmonic Metasurfaces Based on Nanoconvexity

Обучающийся / Student Середин Альберт Артурович
Факультет/институт/кластер/ Faculty/Institute/Cluster физический факультет
Группа/Group Z42761
Направление подготовки/ Subject area 16.04.01 Техническая физика
Образовательная программа / Educational program Техническая физика / Physics and engineering 2021
Язык реализации ОП / Language of the educational program Русский, Английский
Статус ОП / Status of educational program МОП
Квалификация/ Degree level Магистр
Руководитель ВКР/ Thesis supervisor Барышникова Ксения Владимировна, кандидат физико-математических наук, Университет ИТМО, физический факультет, старший научный сотрудник

Обучающийся/Student			
	Документ подписан		Середин Альберт Артурович
	Середин Альберт Артурович		
	25.05.2023		
	(эл. подпись/ signature)		(Фамилия И.О./ name and surname)

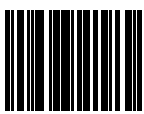| Руководитель ВКР/ Thesis supervisor			
	Документ подписан		Барышникова Ксения Владимировна
	Барышникова Ксения Владимировна		
	25.05.2023		
	(эл. подпись/ signature)		(Фамилия И.О./ name and surname)

Министерство науки и высшего образования Российской Федерации
ФЕДЕРАЛЬНОЕ ГОСУДАРСТВЕННОЕ АВТОНОМНОЕ ОБРАЗОВАТЕЛЬНОЕ
УЧРЕЖДЕНИЕ ВЫСШЕГО ОБРАЗОВАНИЯ
НАЦИОНАЛЬНЫЙ ИССЛЕДОВАТЕЛЬСКИЙ УНИВЕРСИТЕТ ИТМО
ITMO University

АННОТАЦИЯ
ВЫПУСКНОЙ КВАЛИФИКАЦИОННОЙ РАБОТЫ
SUMMARY OF A GRADUATION THESIS

Обучающийся / Student Середин Альберт Артурович
Факультет/институт/кластер/ Faculty/Institute/Cluster физический факультет
Группа/Group Z42761
Направление подготовки/ Subject area 16.04.01 Техническая физика
Образовательная программа / Educational program Техническая физика / Physics and engineering 2021
Язык реализации ОП / Language of the educational program Русский, Английский
Статус ОП / Status of educational program МОП
Квалификация/ Degree level Магистр
Тема ВКР/ Thesis topic Моделирование фотолюминесценции в плазмонных метаповерхностях на основе нановыпуклостей / Simulation of Photoluminescence in Plasmonic Metasurfaces Based on Nanoconvexity
Руководитель ВКР/ Thesis supervisor Барышникова Ксения Владимировна, кандидат физико-математических наук, Университет ИТМО, физический факультет, старший научный сотрудник

ХАРАКТЕРИСТИКА ВЫПУСКНОЙ КВАЛИФИКАЦИОННОЙ РАБОТЫ
DESCRIPTION OF THE GRADUATION THESIS

Цель исследования / Research goal
To build the models of plasmonic metasurfaces based on nanoconvexity covered with HgTe quantum dots for explanation of experimental results for linear scattering and photoluminescence.
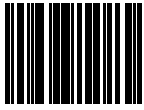**Задачи, решаемые в ВКР / Research tasks**
1. Simulate a model taking into account geometrical parameters given by SEM figures. 2. Find eigenfrequencies corresponding to plasmonic modes and determine their quality factors (Q-factor). 3. Analyze the reflection coefficient spectra for different geometry parameters. 4. Simulate the photoluminescence of a periodic plasmonic array. 5. Make conclusions about the origin of observed modes and compare the results of numerical simulation with experimental data.
Краткая характеристика полученных результатов / Short summary of results/findings
The simulation results assisted to explain the experiment data. It was shown that plasmon mode in the IR range linearly depends on geometric parameters of structure: the height of the jet h, the spacer thickness Al2O3, period d. Moreover, it has been proven that the plasmonic mode supported by the metasurface in the IR range is qBIC, due to which the Q-factor of the mode reaches 70-80. The finite array modeling method quantitatively and qualitatively explains the behavior of metasurface photoluminescence. As shown by numerical simulation and experiment, the optimal thickness of the Al2O3 spacer is d=10 nm. It follows from the far-field radiation

pattern that the plasmonic metasurface emits predominantly in the range of angles from 15° to 35°, the maximum photoluminescence is reached at 17°. In fact, the mode is also observed for a single microbump, however, due to the absence of collective grating effects, the mode is shifted towards longer wavelengths.

Обучающийся/Student

Документ подписан	
Середин Альберт Артурович	
25.05.2023	

(эл. подпись/ signature)

Середин Альберт Артурович

(Фамилия И.О./ name and surname)

Руководитель ВКР/ Thesis supervisor

Документ подписан	
Барышникова Ксения Владимировна	
25.05.2023	

(эл. подпись/ signature)

Барышникова Ксения Владимировна

(Фамилия И.О./ name and surname)

Министерство науки и высшего образования Российской Федерации
ФЕДЕРАЛЬНОЕ ГОСУДАРСТВЕННОЕ АВТОНОМНОЕ ОБРАЗОВАТЕЛЬНОЕ
УЧРЕЖДЕНИЕ ВЫСШЕГО ОБРАЗОВАНИЯ
НАЦИОНАЛЬНЫЙ ИССЛЕДОВАТЕЛЬСКИЙ УНИВЕРСИТЕТ ИТМО
ITMO University

**ЗАДАНИЕ НА ВЫПУСКНУЮ КВАЛИФИКАЦИОННУЮ РАБОТУ /
OBJECTIVES FOR A GRADUATION THESIS**

Обучающийся / Student Середин Альберт Артурович
Факультет/институт/кластер/ Faculty/Institute/Cluster физический факультет
Группа/Group Z42761
Направление подготовки/ Subject area 16.04.01 Техническая физика
Образовательная программа / Educational program Техническая физика / Physics and engineering 2021
Язык реализации ОП / Language of the educational program Русский, Английский
Статус ОП / Status of educational program МОП
Квалификация/ Degree level Магистр
Тема ВКР/ Thesis topic Моделирование фотолюминесценции в плазмонных метаповерхностях на основе нановыпуклостей / Simulation of photoluminescence in plasmonic metasurfaces based on nanoconvexity
Руководитель ВКР/ Thesis supervisor Барышникова Ксения Владимировна, кандидат физико-математических наук, Университет ИТМО, физический факультет, старший научный сотрудник

Основные вопросы, подлежащие разработке / Key issues to be analyzed
Objective: to build the models of plasmonic metasurfaces based on nanoconvexity covered with quantum dots for explanation of experimental results for linear and nonlinear optical scattering
Plan of work:
1. Geometric construction. Compose a model from a SiO2 substrate on top of which conical gold elements 50 nm thick are deposited. The frame period varies from 0.9 um to 1.0 um. Also, plasmonic arrays have a jet at the top of the cones, the height of which varies from 0 to 320 nm. A film of Al2O3 is applied over the metasurface, the thickness of which also varies from 0, 10, 20, 30, 40 nm.
1.1 Simulate a single cell of a periodic array without a field source. Find eigenfrequencies corresponding to LSPR and determine their quality factors (Q-factor). Plot dispersion curves from the Bloch vector.
1.2 Modela periodic array irradiated by the plane wave source. Analyze the dependence of the reflection coefficient on the wavelength of the incident radiation for different geometry parameters: structure period, jet height, spacer thickness. Detect LSPR and SPP and identify them by field distribution.
1.3 With the same parameters of the periodic structure, achieve consistent results for both models (all resonance peculiarities of reflection/absorption spectra have to correspond to eigenmodes of the structure).
2. Simulate the photoluminescence of a finite-sized plasmonic periodic array with a size of 5x5 cells. As a source of radiation, use an electric point dipole placed on top of the central periodic element. The amplitude of such dipole radiation will be related to the photoluminescence

spectrum of quantum dots in solution (experimental data).

2.1 By changing the position and direction of the dipole and the wavelength of the radiation, obtain a photoluminescence spectrum of the plasmonic metasurface for various geometric parameters.

2.2.Study the radiation pattern and the Purcell effect for various geometric parameters.

2.3 Build a self-consistent model describing discrepancies between the photoluminescence spectrum and the reflection spectrum

3. Specify geometric parameters to achieve a good comparison with the experimental results for both reflectance and photoluminescence spectra.

4. Give recommendations to achieve higher values of photoluminescence with similar geometries.

Literature:

[1] Vaskin, Aleksandr, Kolkowski, Radoslaw, Koenderink, A. Femius and Staude, Isabelle. "Light-emitting metasurfaces" Nanophotonics, vol. 8, no. 7, 2019, pp. 1151-1198. https://doi.org/10.1515/nanoph-2019-0110

[2] Stankevicius, E., Vilkevicius, K., Gedvilas, M., Buzavaite-Verteliene, E., Selskis, A., Balevicius, Z., Direct Laser Writing for the Formation of Large-Scale Gold Microbumps Arrays Generating Hybrid Lattice Plasmon Polaritons in Vis–NIR Range. Adv. Optical Mater. 2021, 9, 2100027. https://doi.org/10.1002/adom.202100027

[3] Pavlov, Dmitrii & Zhizhchenko, Alexey & Pan, Lei & Kuchmizhak, Aleksandr. (2022). Tuning Collective Plasmon Resonances of Femtosecond Laser-Printed Metasurface. Materials. 15. 1834. 10.3390/ma15051834.

Дата выдачи задания / Assignment issued on: 15.01.2023

Срок представления готовой ВКР / Deadline for final edition of the thesis 20.05.2023

Характеристика темы ВКР / Description of thesis subject (topic)

Тема в области фундаментальных исследований / Subject of fundamental research: да / yes

Тема в области прикладных исследований / Subject of applied research: нет / not
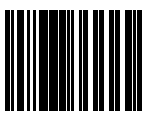
СОГЛАСОВАНО / AGREED:

Руководитель ВКР/ Thesis supervisor	Документ подписан		Барышникова Ксения Владимировна
	Барышникова Ксения Владимировна		
	10.03.2023		

(эл. подпись)

Задание принял к исполнению/ Objectives assumed BY	Документ подписан		Середин Альберт Артурович
	Середин Альберт Артурович		
	20.03.2023		

Руководитель ОП/ Head
of educational program

Белов Павел
Александрович

Руководитель ОП/ Head
of educational program

CONTENTS

INTRODUCTION

There is a need for inexpensive IR radiation sources and receivers. [1]. Quantum dots (QDs) in combination with plasmonic metasurfaces can solve this consumer problem. The chemical synthesis of colloidal quantum dots (CQDs) is already a scalable and relatively cheap technology. In the visible region, QD emission has already been implemented, and the technology is actively used in production (for example, TV matrices) [2]. However, there are a number of difficulties with QDs in the IR range, in particular, low quantum yields and a high spontaneous emission width of 100–200 nm. However, QDs are still considered a promising material for the range of 1.5 - 3 μm. Accordingly, research in this area and further optimization is an urgent challenge. An appropriate metasurface is also needed, which would support plasmon modes in the IR range, and by changing the geometric parameters of the structure, it would be possible to control the narrow-band amplification of QD radiation in the IR range.

The group of A.A. Kuchmizhak (Institute of Automation and Control Processes of the FEB RAS) experimentally demonstrated the optical properties of the metasurface driven by plasmonic effects (Figure 1) in the infrared wavelength range. As shown in the literature review, the Au microbumbs were formed by the method of direct femtosecond laser writing. In addition to the gold microbumps themselves, an Al_2O_3 spacer layer will also be applied to avoid quenching of photoluminescence. Using the distribution of the plasmon mode field, it is possible to increase the enhancement factor of photoluminescence of quantum dots (HgTe) from the plasmonic metasurface. To study photoluminescence, an experiment on pumping quantum dots with a laser was conducted at a wavelength of 685 nm. The HgTe QD was synthesized by the group A.L. Rogach (City University of Hong Kong). Three main dependencies were experimentally studied:

1) Dependence of plasmon dip position on geometry parameters.

2) How are these dips related to the position of the photoluminescence peak of HgTe QD

3) Directivity of photoluminescence radiation

Based on the experimental data, in particular on the SEM image of the metasurface (Figure 1) it is necessary to build a numerical model, simulate the same processes that occur in the experiment, and give a qualitative and quantitative assessment of the obtained results. Thus, we can formulate the goal and objectives of this paper.

Research aim: to build the models of plasmonic metasurfaces based on nanoconvexity covered with HgTe quantum dots for explanation of experimental results for linear scattering and photoluminescence.

Tasks:

1.   Simulate a model taking into account geometrical parameters given by SEM figures.

2.   Find eigenfrequencies corresponding to plasmonic modes and determine their quality factors (Q-factor).

3.   Analyze the reflection coefficient spectra for different geometry parameters.

4.   Simulate the photoluminescence of a periodic plasmonic array.

5.   Make conclusions about the origin of observed modes and compare the results of numerical simulation with experimental data.
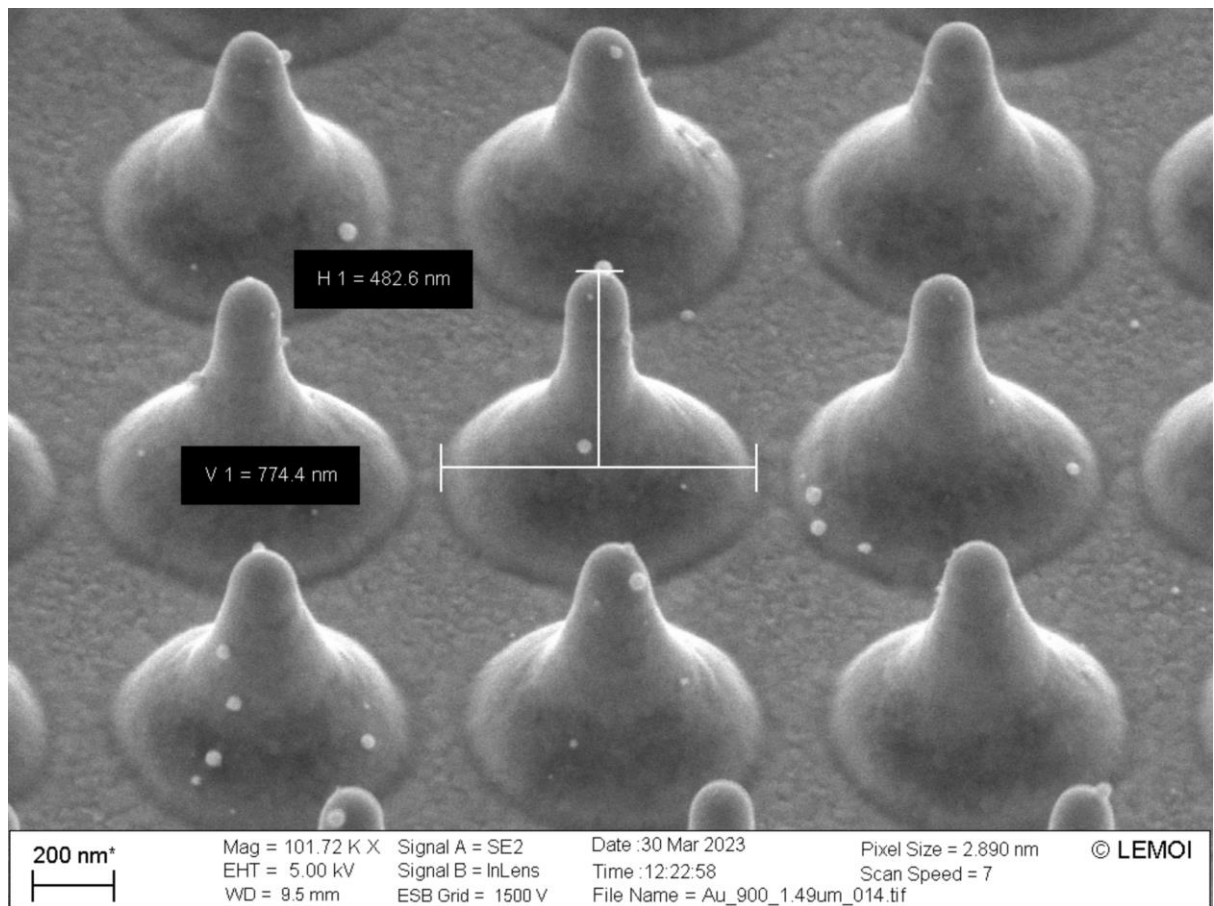
Figure 1 - SEM image of a plasmonic metasurface

1. Literature review

1.1 Plasmonic nanostructures for photoluminescence signal enhancement

Researchers have concentrated on straightforward nanoantenna-based fluorescence signal amplification for the past 10 to 20 years [3]. Current research has directed its attention towards the characterization and optimization of fluorescence enhancement on a singular nanoantenna scale. Attaining this objective necessitates a high degree of technological precision in generating a hotspot. Focused ion beam lithography is an excellent technique for accomplishing such a task [4]. Upon exposure of the antenna-in-box to a solution containing fluorophores, it has been observed that the gap junction of the antenna-in-box can accommodate dye molecules. Additionally, the surrounding nanoaperture box serves as an efficient barrier against background dye molecules that may diffuse away from the junction, thereby leading to a remarkable 1100-fold increase in fluorescence, as depicted in Figure 2 (a) [5]. Furthermore, the associated molecular dynamics were investigated through fluorescence correlation spectroscopy in order to characterize the detection volume and intensity for each emitter. As a result, the study found that detection volumes as low as approximately 60 zeptoliters and molecule count rates exceeding 300 kilohertz were achieved, significantly surpassing the measurements obtained in the absence of the antenna. One promising nanostructure is the patch antenna. This is a nanoparticle on a mirror, it consists of a metal disk and a metal plane. The emitters are arranged in such an order that the vertical spacing between them is maintained. Obtaining gaps less than 10 nm, it is possible to achieve higher Purcell coefficients [6-8]. A real example is a nanostructure, which is a patch antenna made of a film of Au/Ag nanocubes. With such a metasurface, it was possible to achieve a highly effective enhancement factor more than 2000 (Figure 2 (b)) [9]. In addition to the high quantum efficiency that the structure described above demonstrates, there is also a certain change in the direction of the radiation. In particular, the radiation is simultaneous, which is a great advantage. The duration of spontaneous emission in a system of metal nanocubes connected to a film, where the emitters are located

in the region of the dielectric gap, was determined to be less than 0.7 ns due to the time-resolved fluorescence characteristic. Compared to the previous duration of ~500 ns, this is a significant reduction. It also follows from the data that the quantum efficiency exceeded 0.5. Thus, the combination of quantum dots and a patch antenna resulted in a significant increase in the frequency of spontaneous emission (~900) and total fluorescence (~2300), as reported in reference [10].
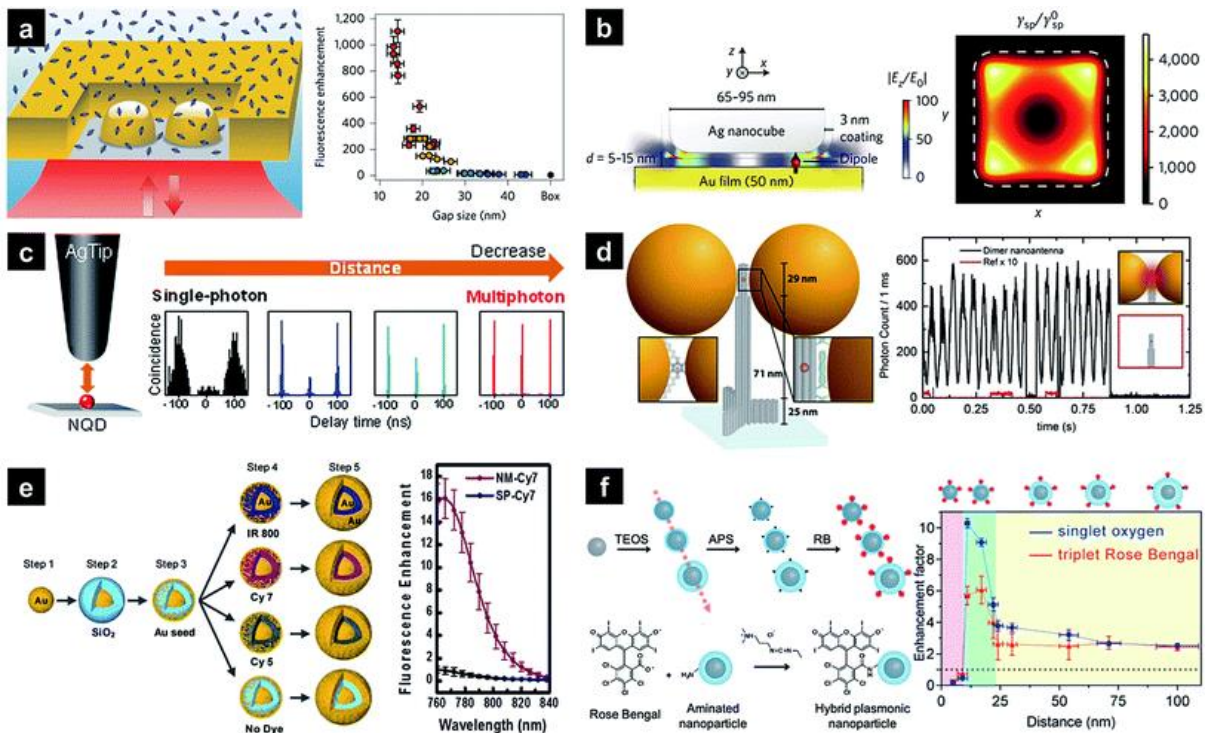

Figure 2 - Plasmonic nanostructures, which enhancing photoluminescence (PL). (a) plasmonic 'antenna-in-box'. (b) Gold film with a silver nanocube patch antenna that contains embedded dyes. (c) The atomic force microscopy tip is coated with silver and contains a single quantum dot. (d) The assembly of dimeric gold nanoparticles is synthesized using a DNA origami technique. (e) The Au nanomatryoshka with dyes. (f) The core-shell nanoparticles consist of Ag-Silica with photosensitizers [4]

The silver tip atomic force microscope system supports the existence of Localized Surface Plasmon Resonance (LSPR). Accordingly, if a quantum dot is placed on the substrate, the effect of photoluminescence modulation can be observed. That is, the PL modulation will occur due to the distance between the needle and the quantum dot, as well as the spectral overlap (Figure 2 (c)) [11]. As

the distance between the quantum dot and the silver tip increased, the emission of multiple photons with a shorter lifetime turned into the emission of single photons with a longer lifetime. This effect is due to the fact that the energy that is transferred from the quantum dot to the needle was also amplified by the local electric field of the tip due to the LSPR. Accordingly, this leads to an increase in intensity. This method is quite inexpensive, and also technologically simple. Plasmonic nanoparticles that are singular in nature can serve as efficient nanoantennae for Surface-Enhanced Raman Spectroscopy (SEF). This is demonstrated by nanorods, which possess a highly adjustable Localized Surface Plasmon Resonance (LSPR) band and a potent local field at their tips due to the lightning rod effect. Let us consider a system that represents Au nanorods immobilized on a glass surface. With a solution of a fluorophore solution, a significant increase in excitation rate gains up to 130 and emission rate gains up to about 10 can be observed. In turn, this leads to an overall increase in photoluminescence (by 1000). Such an achievement is comparable to the results that have been obtained by lithography methods as reported in reference [12]. However, this enhancement is accompanied by the fact that the SPR wavelength must not deviate from the excitation wavelength. In a recent study, the fluorescence dependence on distance and plasmon wavelength was systematically investigated using Au nanorods coated with silica and infrared dyes. The results showed that the fluorescence was maximally enhanced by a factor of ten. This happened when the absorption band of the dye coincided spectrally with the maximum of the localized plasmon [13]. The phenomenon of plasmonic coupling occurs between nanoparticles. It leads to the generation of a strong near field, which is localized in the nanogap junction between nanoparticles. The use of a self-assembled dimer of Au nanospheres with a gap of about 6 nm resulted in a significant increase in fluorescence, as evidenced by a 600-fold increase, as reported in a previous study [14]. This approach also offers the advantage of being more cost-effective and less complex in design. A nanoantenna with decreased interparticle distances was produced using a custom DNA origami template, resulting in a fluorescence enhancement of up to 5000-fold and the ability to detect single emitters

at a concentration of 25 μM. This is illustrated in Figure 2 (d) [15]. A solitary nanoparticle has the capability to produce a potent near field. According to previous research [16-19], plasmonic couplings based on interior gaps exhibit enhanced and reproducible properties in comparison to couplings that rely on strong interactions between nanoparticles. In particular, we can consider the structure of the nanomatryoshka, in which these bonds are supported. The nanomatryoshka consists of a concentric core and a shell. They are isolated from each other by a dielectric gap. The strong bond between the core and the shell leads to the generation of concentrated radiation in the gap region, and this, in turn, leads to an increase in the emitter fluorescence. According to preliminary experimental studies of this particular structure, it was found that the greatest increase in fluorescence intensity, which is wavelength dependent, is achieved when the localized surface plasmon resonance (LSPR) wavelength and the fluorophore excitation wavelength are spectrally matched, [17]. Systematic modeling in the time domain has shown that it is possible to achieve an improvement factor of over 1500 for a golden matryoshka [20]. Achieving the maximum fluorescence signal occurs at peak near-field amplification, resulting in a 16-fold intensity jump as shown in Figure 2(e). Moreover, the strong plasmonic coupling phenomenon can also be demonstrated in the infrared range. In particular, a recent study showed that the introduction of a nanostructured gold array can effectively enhance the second near infrared (NIR-II; 1000–1400 nm) fluorescence signal of Ag_2S quantum dots [21]. This resulted in a significant 100-fold increase in fluorescence at an emission wavelength of 1200 nm.

1.2 Quantum dots. HgTe

It is imperative to acknowledge the primary classification of quantum dots, colloidal quantum dots (CQDs). Over the last ten years, colloidal quantum dots (CQDs) have been extensively investigated for their potential use in optoelectronic and light-emitting applications. Unlike fluorescent dyes and phosphors, CQDs exhibit narrow and tunable emission spectra, making them well-suited for

applications requiring pure, bright and stable emission spanning over visible to IR wavelengths. The ultraviolet and visible spectra are encompassed by the typical cadmium and zinc-based colloidal quantum dots (CQDs) [22]. The lead chalcogenides have demonstrated the ability to achieve tunability in the near-infrared (near-IR) region, with PbSe achieving wavelengths of up to 4 μm [23]. One noteworthy material for CQD that has the potential to emit radiation across a broad range of wavelengths is the semimetal HgTe. By adjusting its size, HgTe can effectively cover the entire mid-infrared (mid-IR) range, as reported in reference [24].
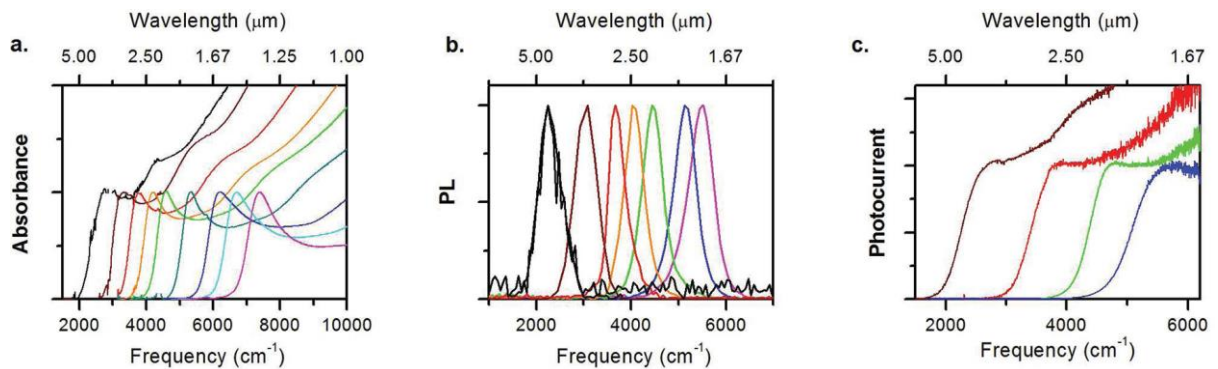

Figure 3 - Normalized spectra. (a) The present study investigates the absorption of solutions containing HgTe colloidal quantum dots in the solvent C_2Cl_4. To enhance clarity, the C-H absorbance originating from the ligands has been eliminated. (b) Photoluminescence of HgTe CQDs in C_2Cl_4. (c) Photoconduction spectra of films of colloidal HgTe nanoparticles of different sizes [24]

The visual representations and analytical results of transmission electron microscopy (TEM) images and X-ray diffraction (XRD) data are presented in Figure 3. The diffraction analysis indicates that the crystal structure of zinc-blende (ZB) HgTe is characterized by well-defined peaks. The particles often exhibit a triangular or distorted parallelogram shape, which is in accordance with tetrahedral geometries. At low temperatures where the growth rates on different faces are dissimilar, the ZB nanocrystals tend to adopt a tetrahedral morphology. The sample illustrated in Figure 4 exhibits a mean edge length of roughly 14.5 nm, which is determined by measuring the length of the edges of the triangular shape. Additionally, the PL peak position of

15

the sample is observed to be at 2460 cm^{-1} (0.305 eV). The triangular particles display a lattice spacing of 0.37 nm, which corresponds to the separation between {111} planes in ZB HgTe. This material has a lattice constant of 6.46 Å.
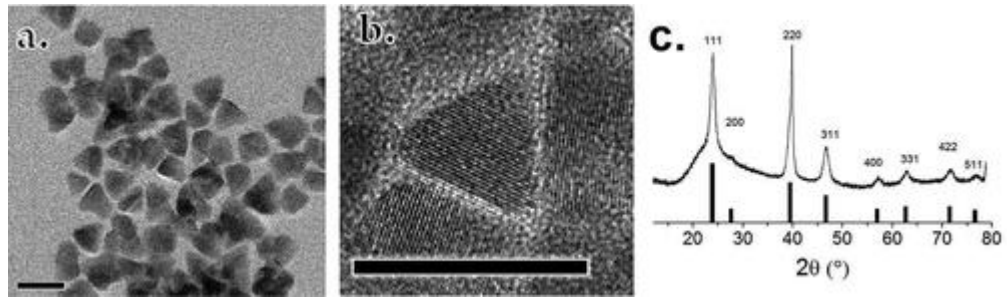

Figure 4 - (a) The transmission electron microscopy image depicts HgTe nanoparticles exhibiting a photoluminescence peak in the vicinity of 2460 cm^{-1} (0.305 eV). (b) The high-resolution transmission electron microscopy (HRTEM) image displays a single particle with an interplanar spacing of 0.37 nm. The scale bars utilized in this study have a measurement of 20 nanometers. (c) The X-ray diffraction (XRD) spectrum featuring prominently labeled diffraction angles of bulk HgTe has been documented [24]

1.3 Plasmonic bound states in the continuum

The intrinsic loss in metals results in a low quality factor of approximately 10, which is a prevalent concern associated with plasmonic resonances [25]. The aforementioned issue poses a limitation on the practical implementation of certain applications, as a considerable number of them necessitate a heightened degree of spectral selectivity. Despite the existence of various metallic nanostructures that can endure narrow surface lattice resonances (SLRs) and enhance the quality factor, their susceptibility to structural imperfections and lighting circumstances is considerably high, as reported in literature [26]. Furthermore, it is common for them to require extensive structured spaces and incorporation within a homogeneous substrate [27]. Subsequently, the field of nanophotonics incorporated BICs, which were originally derived from quantum mechanics [28]. According to reference [29], modes with an infinite Q-factor, known as BICs, in an open system are incapable of coupling to any

radiation channel that propagates beyond the system. Minor disturbances have the ability to disrupt pristine bound states in the continuum (BICs) and produce quasi-BIC modes that possess finite Q-factors, which can be detected in the far field. A variety of photonic applications, such as optical sensing [30], energy conversion [31], and light emission [32], necessitate not only high Q-factors but also durable near-field enhancement and high coupling efficiency. The advantage of plasmonic metasurfaces is the possibility of changing radiation and radiation losses. This is important in that the ultimate factor in optimizing the interaction of light and matter is of paramount importance. However, for dielectric metasurfaces in which there are no non-radiative losses, this feat is unattainable. The discrepancy between their radiation and intrinsic losses does not give them the opportunity to regulate the difference between different energy loss channels [33]. According to reference [34], a significant portion of the incident energy is not effectively coupled to the resonant metasurfaces, resulting in its dissipation as reflection. Symmetry-protected bound states in the continuum (BICs) have been observed in plasmonic metasurfaces, albeit in recent times. However, oblique angles of incidence lead to the fact that the symmetry is broken in the impulse space. At the same time, BICs are sensitive to symmetry breaking. These facts make BICs unsuitable for most technical applications and applications [35]. Thus, a metasurface is needed that would satisfy the following properties: maintenance of modes at normal incidence, strong coupling of light and matter, and the presence of high quality factors. And this is a serious research and technological challenge.

The study presented in [36] demonstrates the development and implementation of a plasmonic nanorib metasurface (PNM) using three-dimensional (3D) laser nanoprinting. PNM consists of a series of equilateral triangular nanofins of the same size and shape. The manufacturing process included the use of a polymer matrix. Next, the entire structure was covered with a layer of gold (as shown in Figure 5 (A)). PNM was developed for molecular sensing. This was facilitated by the presence of several BICs protected from planar symmetry. It is possible to break the PNM out-of-plane symmetry and enter the symmetry-protected quasi-BIC mode

(defined in Figure 5(B)). In particular, the first and second order modes exhibit maximum Q factors of about 100 and 180, respectively. The utilization of the BIC results in an elevation of the radiation Q-factor, whereas the non-radiative Q-factor does not exhibit an infinite behavior. Thus, the overall Q-factor experiences an increase, albeit without reaching an infinite value. The results presented in Figure 5(C) show that absorbance, which is a measure of drive efficiency, and quality factor (PNM) can be flexibly adjusted in parameter space, which in turn allows the PNM coupling mode to be adjusted from undercoupling (UC) to critical coupling (CC) and to over-coupling mode (OC). This happens due to a change in the ratio of radiation and non-radiation losses. It is possible to build such an array that will support all coupling regimes and perform point molecular sensing (Figure 5 (D)). Also, due to the expansion of the spatial parameters of the geometry, it is possible to achieve coverage of wavelengths in the infrared range, namely in the middle infrared range (MIR), a prerequisite for the successful implementation of this surface-enhanced infrared absorption spectroscopy (SEIRAS) technique. The study revealed that quasi-bound states in the continuum (quasi-BICs) can be modulated either negatively, positively, or not at all by molecular analytes. The coupling efficiencies between the light and the PNM pixels used, as shown in Figure 5(E), affect the modulation. Moreover, the rate of radiative decay of the metasurface also affects the value of optimal coupling. Therefore, setting this parameter is as important as high Q-factors and field enhancements.
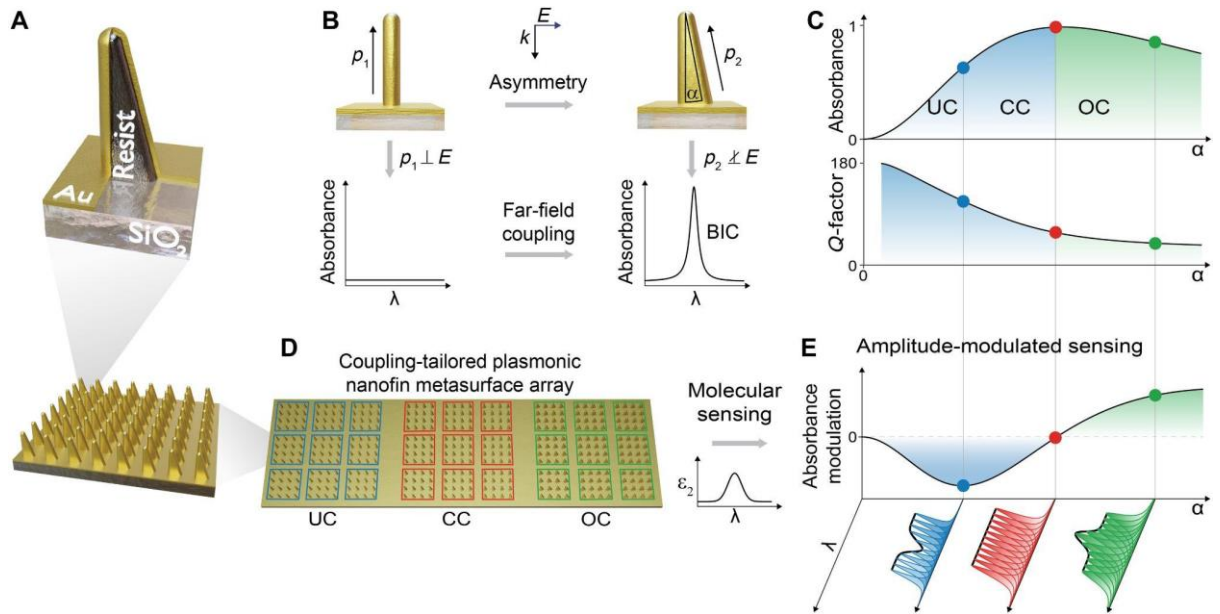
Figure 5 - Plasmonic nanofin metasurfaces (PNMs) (A) Schematic representation of a unit cell of PNM. (B) The object is a dipolar rod that is symmetric and stationary. (C) The adjustment of coupling regimes (D) Schematic representation of a PNM array (E) Relationship between modulation and coupling regimes [36]

The findings of this study indicate the presence of two symmetry-protected bound states in the continuum (BICs), as depicted in Figure 6, with respective wavelengths of 8.3 μm (BIC1) and 4.8 μm (BIC2). These BICs can be converted into quasi-bound states with finite lifetimes by perturbing their inversion symmetry either in momentum or parameter space. The third mode within the range of 3 to 4 μm has been ascribed to an in-plane SLR that exhibits non-dissipative behavior at the point of observation. This mode possesses an incidental bound state in the continuum (BIC) at an angle of = 18°. The subsequent section elucidates that manufacturing and measurement flaws considerably undermine the efficacy of the SLR, as evidenced by the conducted experiments. Upon examination of their mode profiles at the points of maximum absorption in parameter space, as indicated by the red lines in Figure 6 (A). The electric and magnetic field distributions of BIC1, BIC2, and the SLR are illustrated in Figure 6 (B to D). Specifically, the first mode (BIC1) and the second mode (BIC2) exhibit such profiles, with the electric field vectors being perpendicular to the excitation and the magnetic field vectors

circulating around the nanofins and the out-of-plane dipoles are incapable of coupling with the incident light at that particular point due to the dipole moment of the nanofins and the impinging electric field having a scalar product of zero. In comparison to the BIC modes that are out-of-plane, the profile of the SLR mode depicted in Figure 6 (D) bears a resemblance to an in-plane electric dipole. It is characterized by strong electric fields that exist between adjacent nanofins, and an out-of-plane magnetic field that circulates around them. Radiation decay channels are minimized due to the applied gold layer.
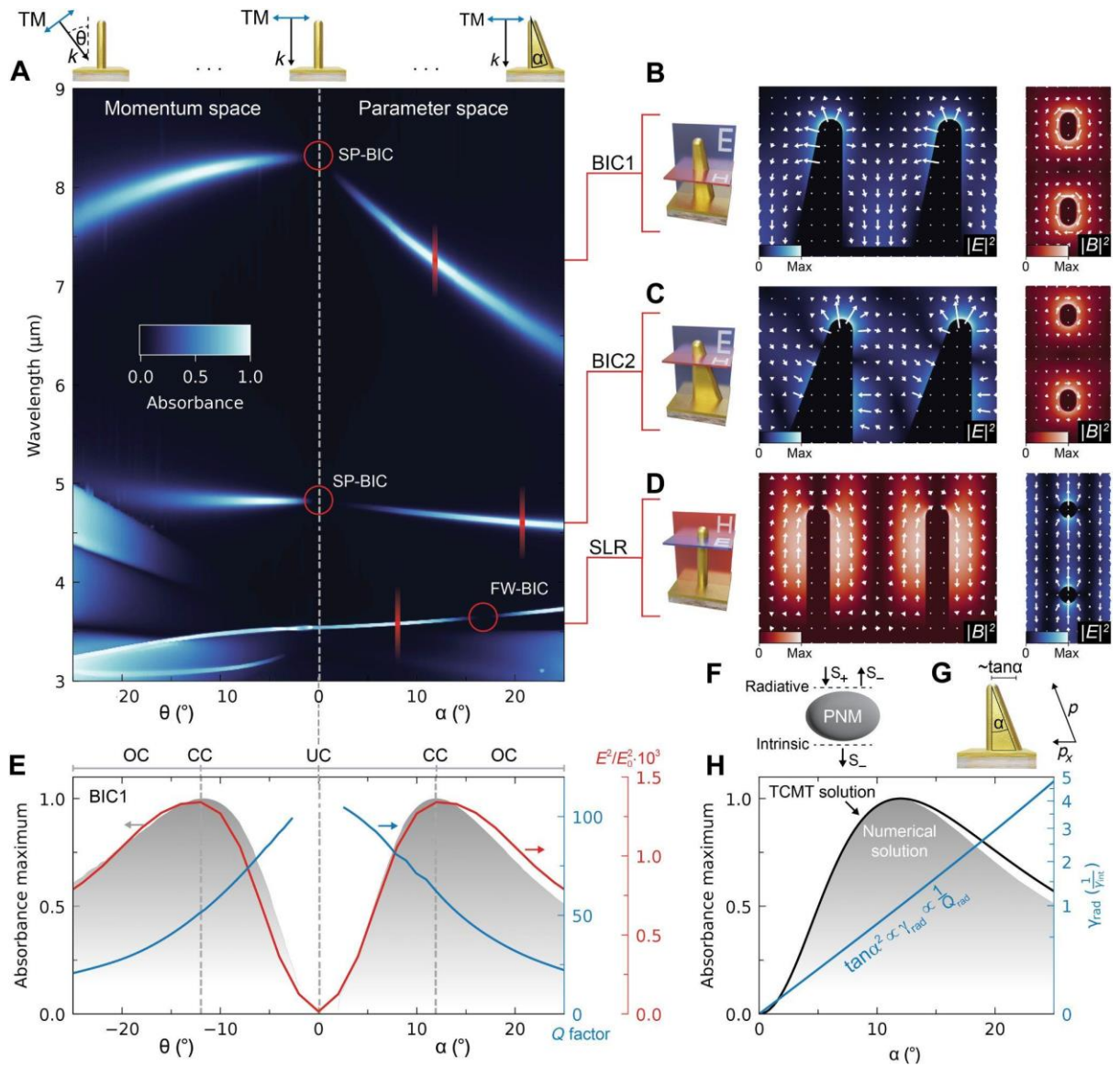
Figure 6 - Numerical analysis of symmetry-protected BICs. (A) Transverse magnetic (TM) absorbance spectrum. (B to D) Field distributions and profiles of modes (E) The maximal absorbance for different coupling regimes. (F) Schematic representation of optical channels in a solitary resonator (G) Relationship between

nanorib symmetry and dipole projection (H) The obtained maximal absorbance (in gray) was numerically compared to the TCMT analytical model (in black) [36]

Figure 6(E) illustrates that the magnitude of the absorption maximum, the quality factor, and the enhancement in the BIC1 surface field for the asymmetry parameters change almost mirror-symmetrically for two different strategies for breaking symmetry. As already mentioned, the tuning process can effectively adjust the parameters and consequently the properties of the mode, resulting in a maximum quality factor of 105 for BIC1 (as shown by the blue curve in Figure 6 (E)).

1.4 General concepts for the analysis of photoluminescence of periodic structures

Besides experimental studies, it is often necessary to predict the optical properties of metasurface such as quality factor, reflection / transmission / absorption spectra, radiation patterns etc.

There is a method for calculating photoluminescence from periodic metasurfaces, which can be implemented both analytically and numerically. This method is based on the principle of reciprocity. The reciprocity principle for magnetic dipole and electric quadrupole sources is formulated by Landau et al. [37], as depicted in Figure 7. The main advantage of this principle is that the far-field power and radiation polarization are calculated in the near-field from a single dipole without including the dipole itself in the numerical calculation.

It is noteworthy that modeling using this method will not allow taking into account dark modes that can potentially exist in the structure. This imposes serious limitations on the applicability of this method. Since it is impossible to quantify emission in controlled modes and quenching.

Another method which is called finite array simulation. This method is not analytical, however it allows you to calculate complex structures and consider dark modes in calculation. Note that an analytical solution can only be presented for

relatively simple geometries, as well as systems with a small set of materials, the refractive index of which depends on the wavelength either weakly or not at all [38]. The problem becomes even more complicated if the system is 2- or 3-dimensional. The finite array method is conventionally employed for the purpose of simulating a metasurface that features a solitary coupled point source [39].
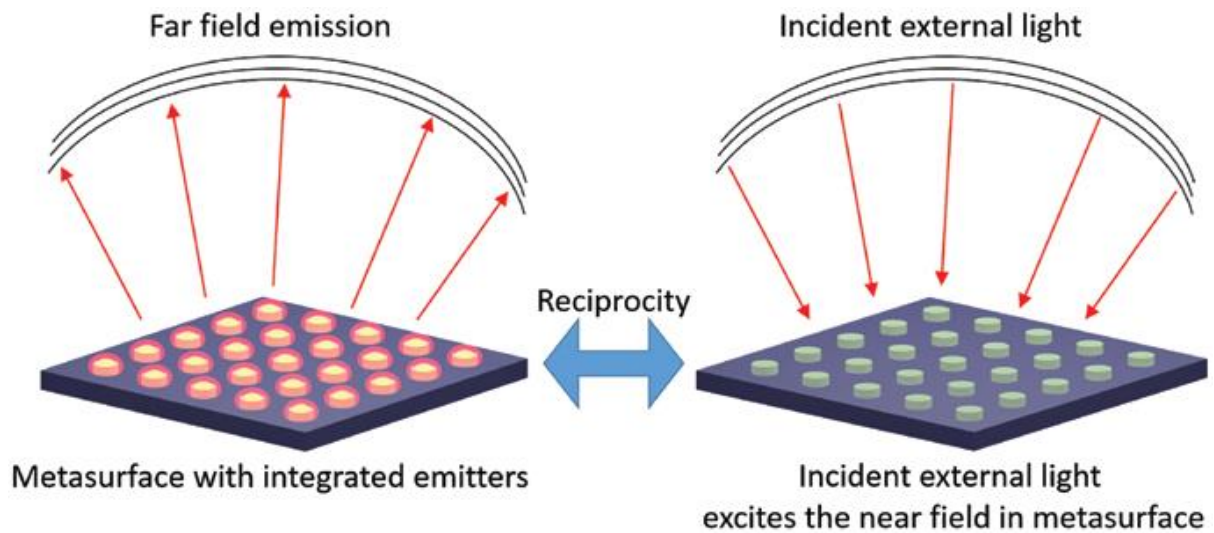

Figure 7 - The reciprocity principle. Correspondence between different systems [38]

Although it is not feasible to simulate the complete periodic structure, it is viable to generate a limited array of unit cells within the computational domain by employing either PML (perfectly matched layer) or open boundary conditions, as illustrated in Figure 8 (A). However, it is necessary to choose such an array size that the solution actually describes the system to some degree of accuracy. This is due to the fact that the computing resource is limited and we cannot choose an infinitely large array. However, if you make an array of a small number of cells, there is a chance that the solution will converge poorly and ultimately not be representative. [39].
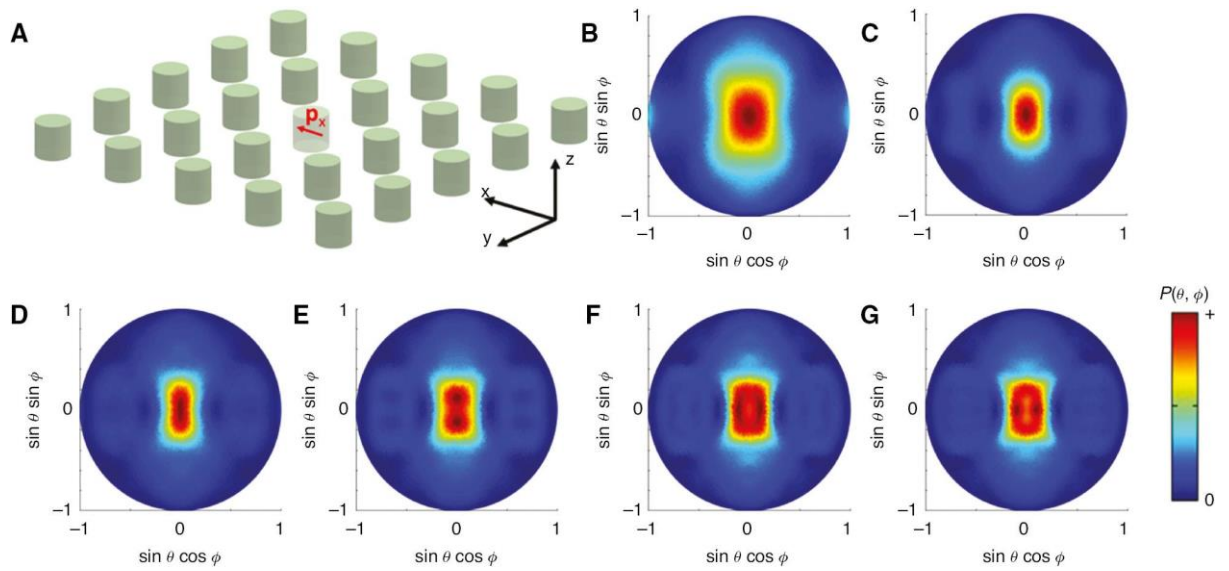
Figure 8 - (A) A finite array comprising of dielectric nanocylinders with dimensions of 5×5 is stimulated by a point electric dipole p_x that is positioned at the center of the central nanocylinder and oriented along the x-axis. The emission pattern $P(\theta, \phi)$ within the upper semisphere $(z>0)$ can be observed from a finite array comprising various unit cell configurations, namely (B) 3×3, (C) 5×5, (D) 7×7, (E) 9×9, (F) 11×11, and (G) 13×13 [38]

The emission patterns $P(\theta, \varphi)$ into the upper hemisphere $(z > 0)$ from a point electric dipole oriented along the x-axis and positioned at the center of a finite array are illustrated in Figure 8 (B–G). The simulation takes place for an array that consists of unit cells with a lattice constant of 1000 nm, and the number of unit cells in the array is gradually increased. The structural unit of the considered material is a nanocylinder with a diameter and height of 400 nm with a refractive index of 3.5. The refractive index of the environment is 1. The oscillations of the electric dipole point correspond to the frequency corresponding to the excitation of the electric dipole resonance of the nanocylinders. As the number of structure elements increases, the pattern of the distribution field undergoes changes. Characteristic change at the beginning with the transition from 3x3 to 5x5 and to subtle changes from 11x11 to 13x13, which indicates the convergence of the solution.

1.5 Formation of Gold Microbumps Arrays. Laser printing

Suppose that there is such a device architecture that satisfies all the requirements for the desired optical signal response, then other questions arise: what is the technological complexity, duration of creation, scalability, and also the cost of the process for synthesizing such devices.

The paper [40] presents the formation of large-scale arrays of gold microprotrusions using direct laser writing. The fabricated arrays exhibit hybrid grating plasmon polaritons in the Vis-NIR (Visible near infrared) range, the same range as metal gratings fabricated by lithography-based techniques. Properties of the hybrid lattice plasmon resonance depend on the period of the fabricated arrays, the thickness of the gold film, the coupled polarization of the light, and the orientation of the sample. This method demonstrates corresponding technological progress in the formation of large-scale metal gratings using an economical laser method.

Using direct laser writing (DLW) with second-harmonic (515 nm) 300-fs laser pulses generated by Yb:KGW-based f-laser (Pharos, Light Conversion Ltd.), large-scale arrays in thin gold films (thickness $\approx$ 50 or 25 nm) were produced. Using an objective with a numerical aperture (NA) of 0.5, the femtosecond laser beam was sharply focused into a 1 μm point. Irradiating a thin gold film with a single pulse results in the formation of a gold microbump, [41] a crucial component of the manufactured grating. Figure 9 (a) depicts the formation of gold lumps during the Au film processing procedure. Each gold bump was manufactured with a single 1.5 nJ laser discharge. To maintain a 0.7 m distance between irregularities in the scanning direction (x-axis), the sample translation speed and pulse repetition rate were set to 2.8 mm s^{-1} and 4 kHz, respectively. By adjusting the translation stage, the distance between bumps in the y-axis direction (perpendicular to beam scanning) was set to 0.7 m.
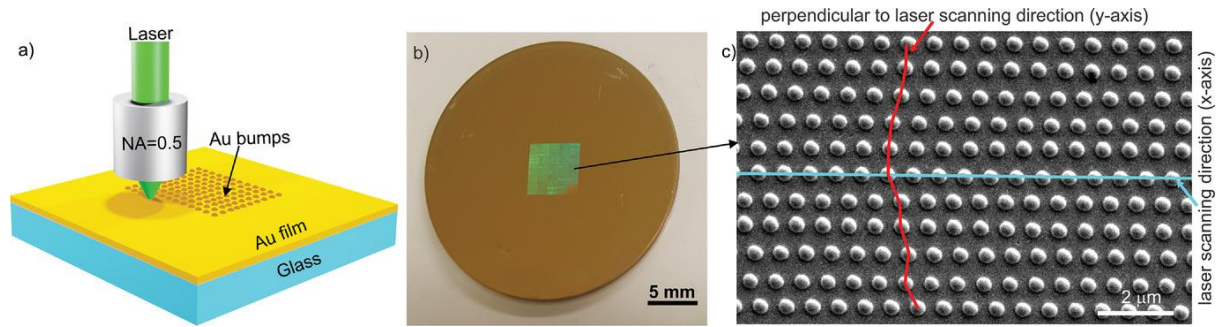
Figure 9 - a) Illustration of Au bumps formation in a thin gold film using direct laser writing technique; b) photograph of large-scale gold microbump grating (5 × 5 mm²); c) SEM micrograph of fabricated gold bumps array in a thin gold film (50 nm) [40]

This formation technique permits a threefold increase in the fabrication speed of the gold bumps array (5×5 mm², Figure 9 (b)) compared to the point-by-point method. Thermal stresses generated in a solid film with laser pulse energy below the melting threshold lead to the formation of gold spikes in the film. The post-irradiation stresses result in deformations of the gold film. During deformation, the film acquires momentum normal to the surface of the substrate. As long as the film remains solid, momentum is extinguished by plastic deformations, which result in the formation of a hump (Figure 9 (c)). [42] Bulgakova has demonstrated that the elastic properties and yield stress of gold completely govern the effect of microbump formation in gold films.

Due to the Gaussian intensity distribution of a laser beam, the majority of the pulse energy is concentrated in the center of the laser beam (Figure 10 (a)). Therefore, the dimension of the manufactured gold bumps is smaller than the laser beam spot (Figure 10 (b)). The cross-sectional SEM micrograph of gold microbumps reveals that each is hollow (Figure 10 (c)). The size of the ridges is dependent on the thickness of the gold film and the laser processing parameters.
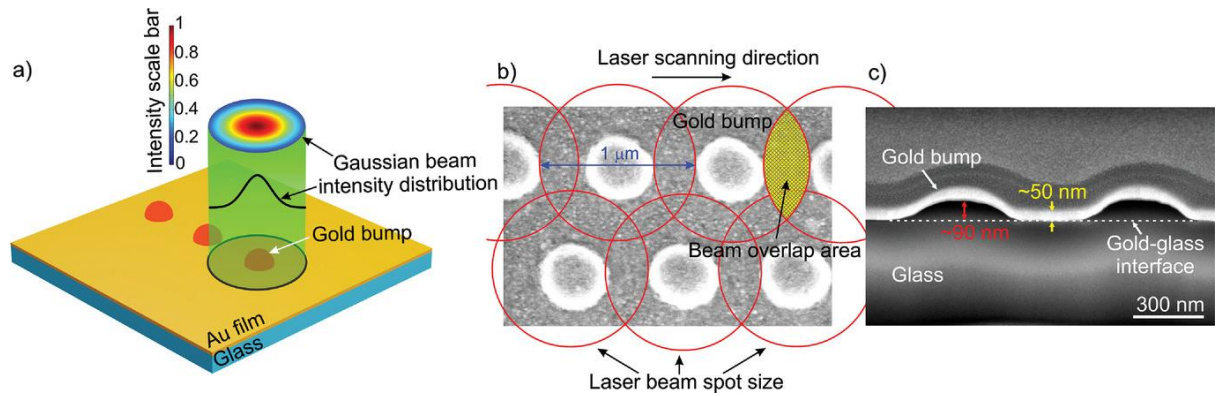
Figure 10 - a) Illustration of the formation process of Au bump; b) the irradiated gold film areas with a laser beam (red circles) in the gold bumps fabrication process; c) SEM micrograph of gold bumps (bright layer) cross-section. The micrograph was taken by coating a thin platinum layer (dark area over the gold bumps) in order to get better contrast at a sample tilt angle of 53° [40]

Using the same laser processing parameters, the diameter of microbumps in 50 and 25 nm gold films is 400 ± 18 nm and 348 ± 15 nm, respectively (Figure 11). The diameters of gold irregularities were measured using image processing and analysis software (ImageJ) to analyze SEM micrographs [43]. The microbump height for 50 and 25 nm thick films is ≈ 140 nm and ≈ 120 nm, respectively. Using the same laser processing parameters, the denser gold film absorbs more laser pulse energy, resulting in the formation of larger microbumps in 50 nm film.
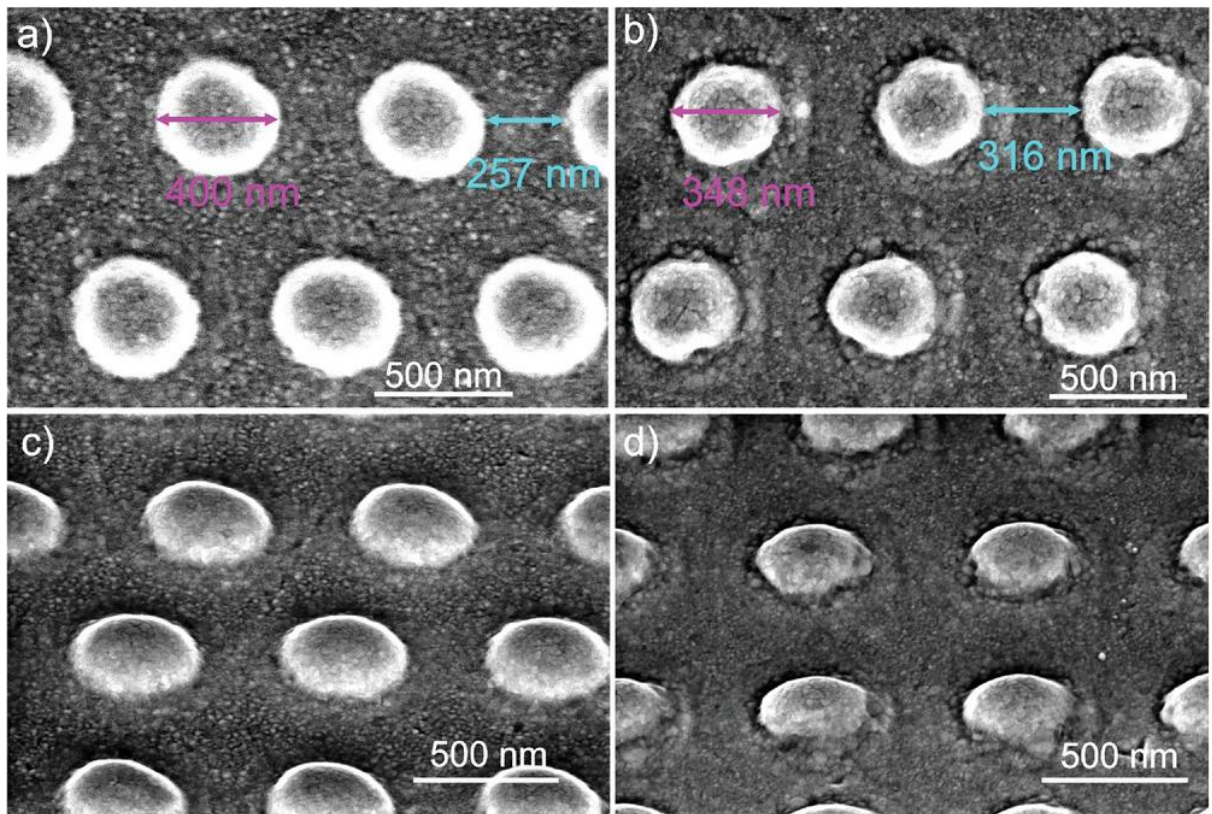
Figure 11 - SEM micrographs of gold microbumps fabricated in Au film with a thickness of a,c) 50 nm and b,d) 25 nm. SEM micrographs depicted in (c) and (d) were taken at a sample tilt angle of 45°. Each microbump was fabricated using a single laser pulse with 1.5 nJ energy [40]
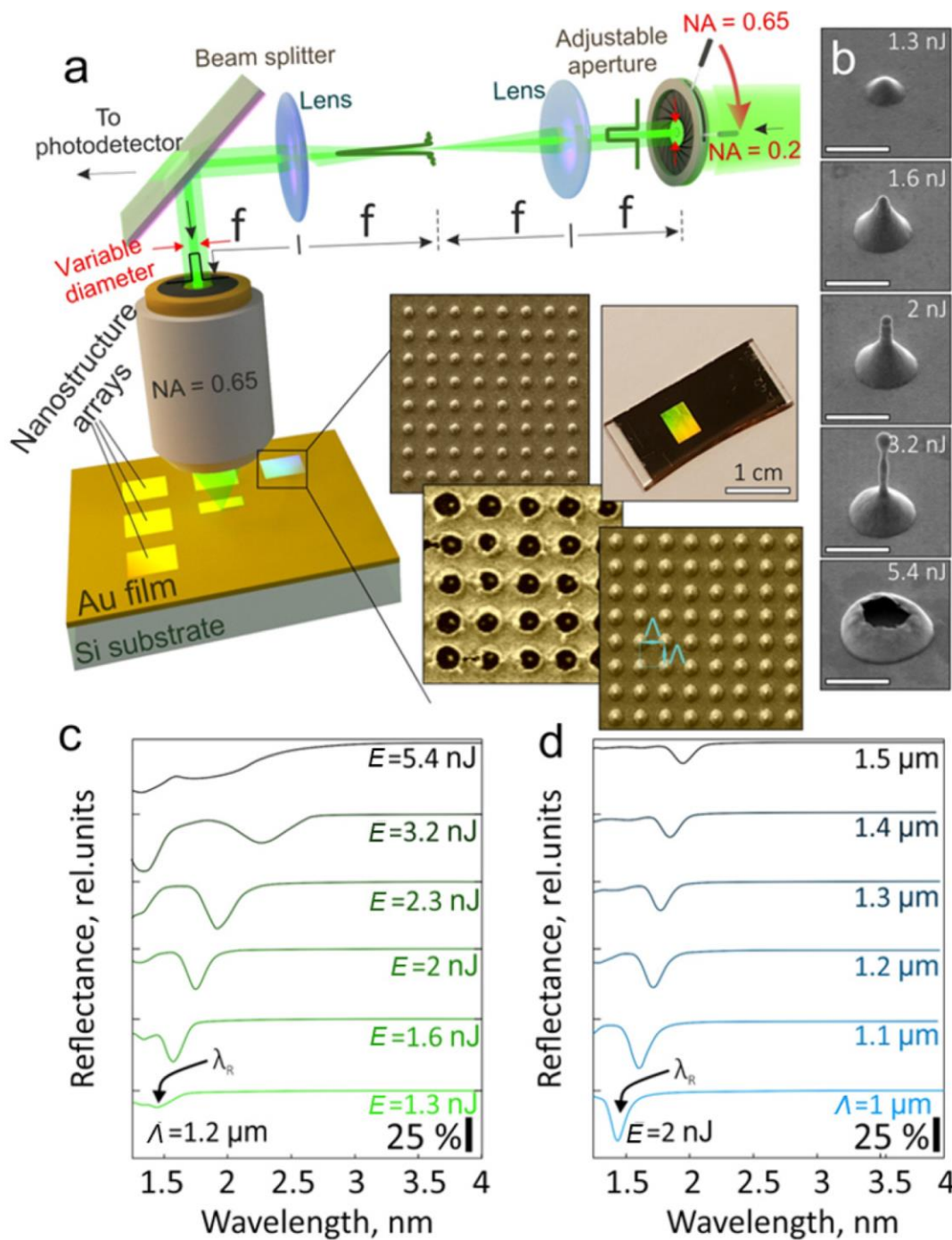
Figure 12 - (a) Schematically illustrated setup for direct laser fabrication of nanostructure arrays using adjustable aperture to control the effective NA of the focusing objective. (b) A set of scanning electron microscope (SEM) images depicting the lateral view of the nanostructures that were isolated at a numerical aperture (NA) of 0.65 and subjected to a range of applied pulse energies between 1.3 and 5.4 nJ. (c,d) The reflectance spectra of the nanostructure arrays were obtained via FTIR analysis. The arrays were produced under conditions of variable

pulse energy E and fixed array period Λ = 1.2 μm (c), as well as variable Λ and

fixed E = 2 nJ (d) [44]

The direct laser printing method is also used in [44]. However, this article demonstrates already the geometric features of nanoconvexities with a change of the laser pulse energy during the fabrication of the structure. The plasmonic response from such a system is already polarization insensitive, in contrast to [40]. And accordingly, for different geometric shapes of nanoconvexities, a series of reflection spectra in the infrared region are given (Figure 12).

Figure 12(b) shows a sequence of SEM images of microbumps that were generated by a femtosecond laser with different pulse energies. It can be seen that with increasing pulse energy, there is a transition from a parabolic bump to a bump with a nanojet. A further increase in energy leads to the destruction of the bumped structure. Based on the FTIR spectra for different arrays of nanostructures (Figure 12 (c)) one can observe the resonance decline [45], which was previously attributed to destructive interference of surface plasmons. It should be noted that the periodic plasmon structure provides effective coupling with surface plasmons (SP) due to the matching of the wave vectors of the incident and surface waves. For a simple film of gold, this is unattainable. As a result, it can be observed that a decrease in the size of the nanostructure leads to a blue shift in the position of collective plasmon resonances (CPR), where the wavelength λR is proportional to the effective period Λ_{eff}. This is due to the fact that the effective period is determined not only by the geometric periodicity of the array Λ, but also by the height of nanojet.

By choosing the appropriate parameters, it is possible to achieve the following results. A CPR quality factor of over 10 and an amplitude of 40% over a relatively wide spectral range from 1.4 to 4.5 μm, as shown in Figure 13(a). The maximum quality factor of 17 (R = 4.23 μm) was achieved with the minimum estimated effective numerical aperture NA = 0.2. The results indicate a significant level of reproducibility of the period of the array and the shape of the nanostructure.
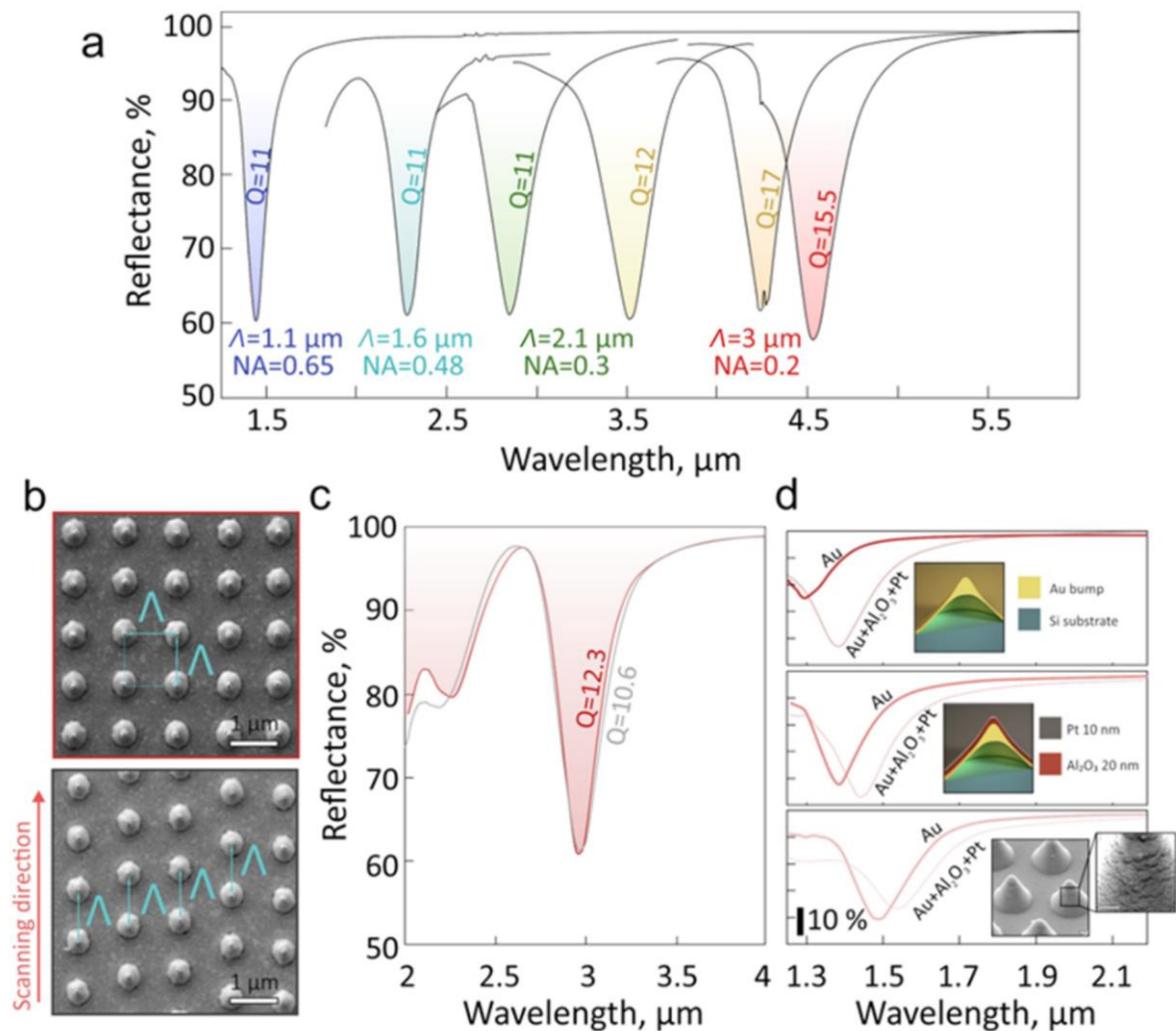
Figure 13 - (a) A collection of FTIR reflection spectra (b) Top-view SEM images of the nanobump arrays (Λ = 2 µm and E = 4.5 nJ) (c) The FTIR reflection spectra of the nanobump arrays. Presence and absence of femtosecond laser synchronization (d) A collection of FTIR reflectance spectra of the nanostructure arrays for different spacer materials [44]

As shown in Figure 13(b), by desynchronizing the laser, the structure can be made disorderly. And then evaluate the contribution of disordering by measuring the FTIR spectra. In Figure 13(c), the array of disordered nanostructures showed a quality factor of 10.6 and the array of ordered structures 12.3, which is slightly larger.

Furthermore, a post-fabrication process can be implemented to optimize the plasmonic characteristics of the nanostructure arrays and enhance the efficiency of

the device. Figure 13 (d) reveals that the plasmonic response of the nanostructure arrays, produced with a fixed $\Lambda = 1$ μm and variable E, remains unaffected by the application of additional layers, as demonstrated by the FTIR reflectance spectra. The act of capping nanolayers can be regarded as a means of modifying the refractive index of the surface plasmon wave that is sustained by the interface of the metal film. This modification leads to a noticeable redshift in the CPR spectral position, as documented in reference [46].

The findings of this study confirm that the creation of plasmonic metasurfaces using the femtosecond laser printing method is promising. Moreover, the technology is potentially scalable and does not require the use of additional chemical methods. The ability to control the position of the plasmon resonance in the infrared range makes it possible to create devices that will be used in sensing, nonlinear optics and optoelectronics and will operate in the IR range (in particular, 1.4–4.5 μm). The presented arrays of nanostructures demonstrate a collective plasmon response that is insensitive to polarization, with a maximum amplitude of 45% and a resonant Q factor of up to 17. It is also possible to study such plasmonic metasurfaces not only based on gold, but also on other noble and semi-noble metals, which also further expands the range of applications. and further research.

2. Methods and materials

2.1 Geometry construction

Analyzing the SEM images of manufactured samples, in particular Figure 13, we can present the following geometry for numerical simulation (Figure 1).
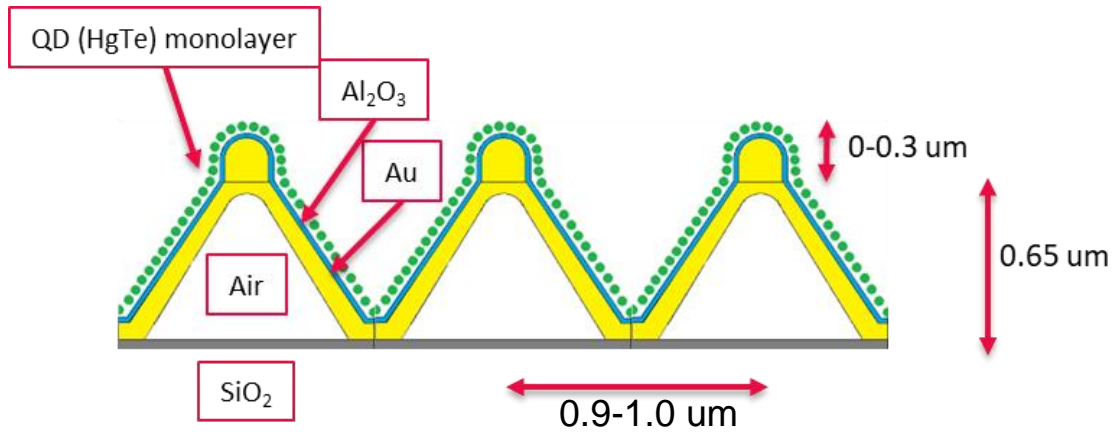
Figure 14 - Schematic representation in profile, materials and geometric parameters

We assume that the sizes of the cones are fixed, namely bottom radius ~ 300 nm, the height of cones ~ 650 nm, and the thickness of gold 50 nm. In the literature review and in the experiment, the dependence of the jet height on the femtosecond laser pulse energy was demonstrated, therefore we will change the height of the jet from 0 to 300 nm. The period of the structure varies from 900 nm to 1000 nm. As mentioned above, an Al_2O_3 spacer is used to increase the effective refractive index, and, accordingly, the effect of film thickness on optical and plasmon processes is also studied, Al_2O_3 spacer thickness varies from 0 nm (no spacer) to 40 nm. The thickness of QD (quantum dots) HgTe monolayer ~ 4-8 nm.

Due to the rather complex structure of the metasurfaces, a suitable research method would be numerical modeling, rather than the analytical description of the model. In numerical simulation of wave processes, finite elements are employed when the entire structure is divided into a small number of subelements (tetraeders, parallelepipeds, and other geometric figures), and the program (in our case - Comsol Multiphysics) solves the Maxwell equations for each element of the grid [47]. The

result of the calculations depends on the size of the grid cell, the convergence of integral values is observed when the maximum size of a grid element is not more than $\lambda/5$, where λ is the wavelength of the electromagnetic field; for the convergency of values considered in the point, the split should be even more substantial, however, this work considers predominantly integral quantities.

In the equation for the amplitude of electrical and magnetic fields, there is a component dependent on time and a component dependent on coordinates. Naturally, if the processes occur in a stationary system, then solve the equation in the stationary case when the dependency on time is harmonious. If transitional and dynamic processes are interesting, then temporary components of fields are included. Concretely, the case investigated in this work is stationary.

In this work, all the simulations were made in Comsol Multiphysics 6.0. Dispersion parameters of materials:

- Gold [48]

- Al_2O_3 [49]

- HgTe QD (figure 14). Experimental data were obtained by the group of A.A. Kuchmizhak and these data are not universal for all HgTe QDs, as the dispersion parameters depend on the synthesis technology.
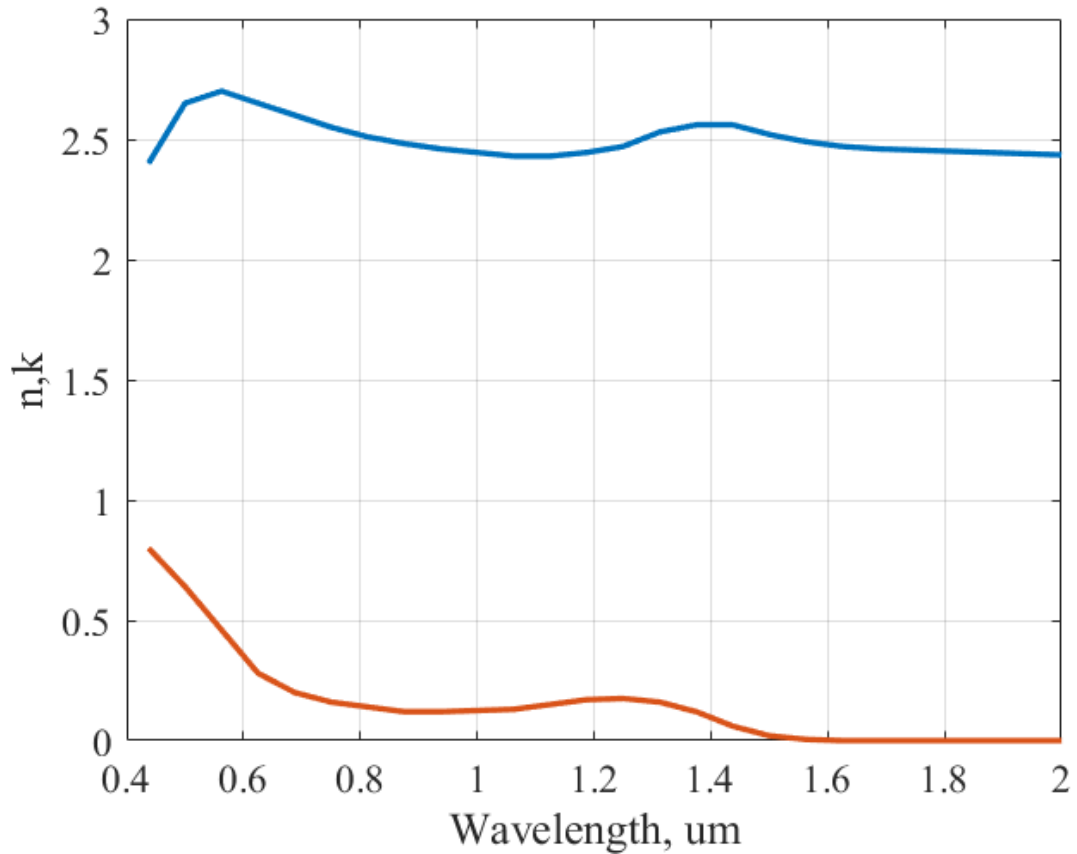
Figure 15 - Dispersion of quantum dots (dependence n, k on the wavelength)

2.2 Modeling. Eigenfrequency

The universal method of studying any system is the study of the eigenmodes of the system. In order to find the system's eigenmodes, we will set the frequency (wavelength), and the program will search solutions in the vicinity of frequencies (wavelengths). Not all of the modes obtained are physical, many modes when calculated will be artifacts of calculation. It is important to separate physical modes from artifacts, this can be done in different ways. The most popular way is to filter by field distribution and the value of the Q-factor. Since the structure is periodic in two directions, we will study one such cell (Figure 16), and the periodicity will be set by periodic boundary conditions of Flocke. For the first zone Brillouin zone (G-X), the value of the Bloch wave vector for the coordinate "x" (k_x) will vary from 0 to π/d, where d - the period of the lattice. You can set scattery boundary conditions or a perfectly matched layer (PML). In the case of scattery boundary conditions, the

calculation speed is higher than with the PML layer. However, the PML condition gives a better convergence of results, so we used it.
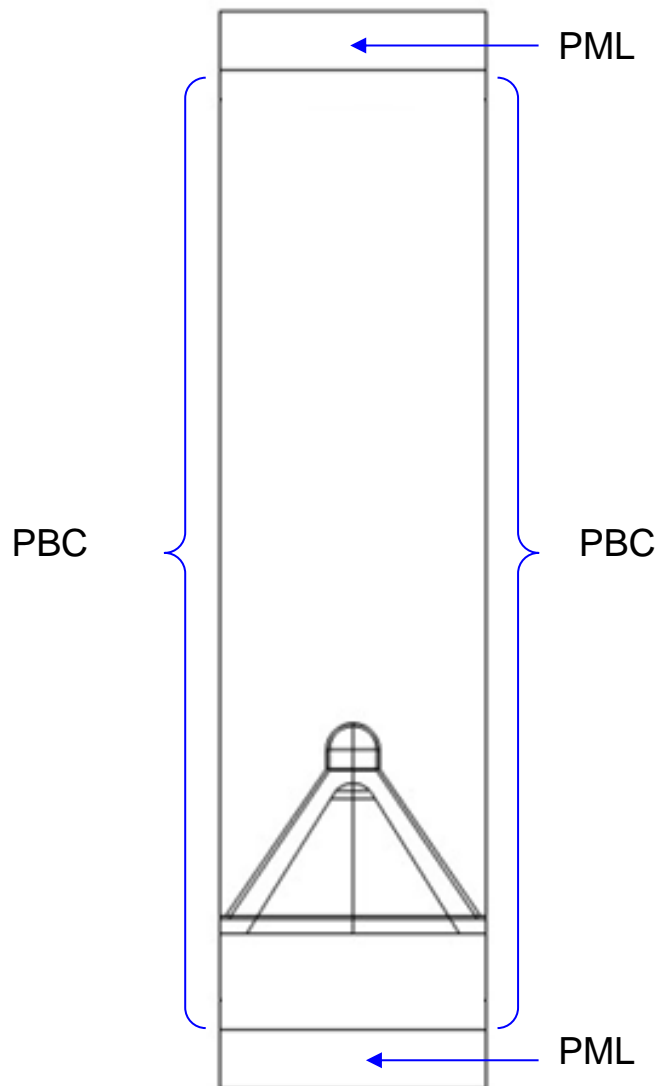

Figure 16 - Microbump profile. Boundary conditions

2.3 Modeling. Reflection spectra

In order to analyze the experimental reflection, transmission, and absorption data and compare them with the obtained eigenmode data, we will continue to solve the problem of excitation when a plane electromagnetic wave is incident. In the calculation, we can set the direction of the wave and the wavelength (by changing the components of the wave vector), as well as the polarization by changing the components of the electric or magnetic field. In this analysis, the dependence of

reflection/transmission/absorption on wavelength will be investigated during the incidence of a plane wave. In order to excite a plasmon-polariton at the metal-dielectric interface, either TE polarization or TM polarization is used [50]. In the case of different ε materials and the same μ, TM polarization is used. Therefore, we will use the Tm polarization in our simulation. Fundamentally, nothing changes in the model scheme compared to the previous paragraph. However, we need to set the source of the plane electromagnetic wave (Port 1 and Port 2) (Figure 17). In this case, Port 1 is the source of an electromagnetic wave, and Port 2 is only a receiver.
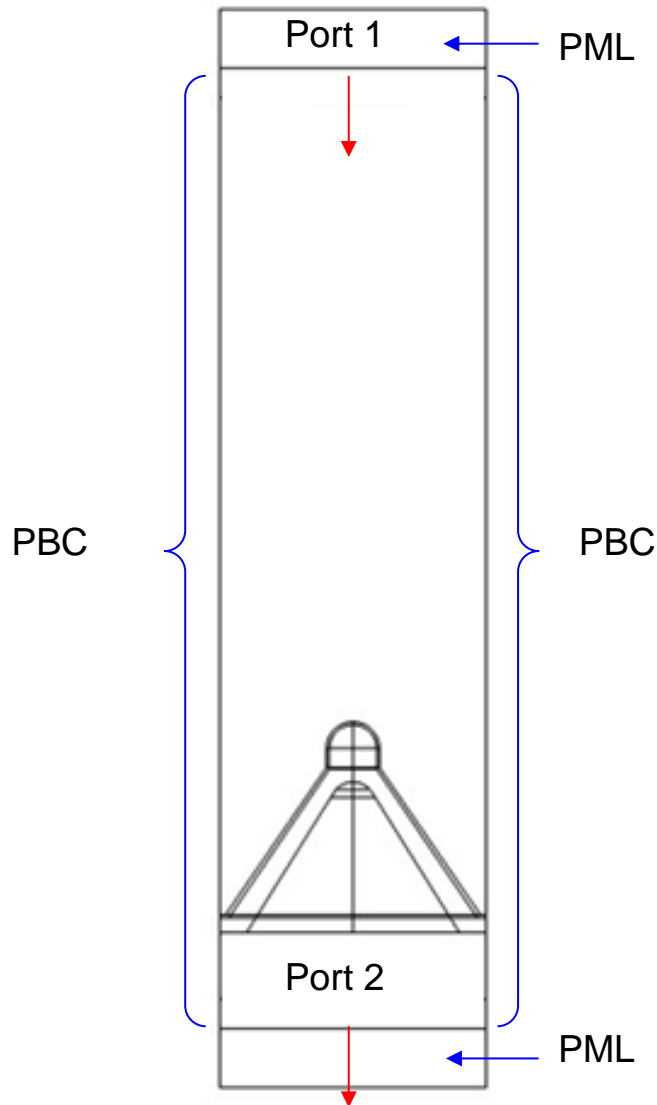
Figure 17 - Microbump profile. Boundary conditions

2.4 Modeling. Photoluminescence

When modeling photoluminescence from such a structure, the finite array simulation method, which was mentioned in the literature review, will be applied [36]. Due to the complex geometry of the model, in particular the presence of thin films, the maximum dimensions of the metasurface mesh elements decrease, which leads to the fact that the total number of mesh elements in the model increases and, consequently, the calculation speed decreases. It is not only about the speed of computing, but also about the size of the operating memory. It was mentioned that the method of modeling a finite array implies the simulation of a small and finite

section of the model, so we cannot infinitely increase the dimension of a model, and ultimately we are limited by the volume of operating memory. In this work, all calculations, including the calculation of photoluminescence, were performed on a computer with 512 GB RAM. For such a relatively large operating memory, the limit of the size of the model is a system of 5x5 cells (Figure 18). The boundary conditions on the surface of the computational sphere are open. The source of the electromagnetic field is a point electric dipole placed in the place of high localization of the plasmon mode for the central element of the metasurface (Figure 18 (inset, red arrow)). Why the jet tip is the site of high-mode localization will be explained in the simulation results. An additional sphere with a high mesh density is also set around the dipole, which helps to significantly reduce the error in calculating the field distribution and radiation directivity (Figure 17 (inset, blue arrow)).
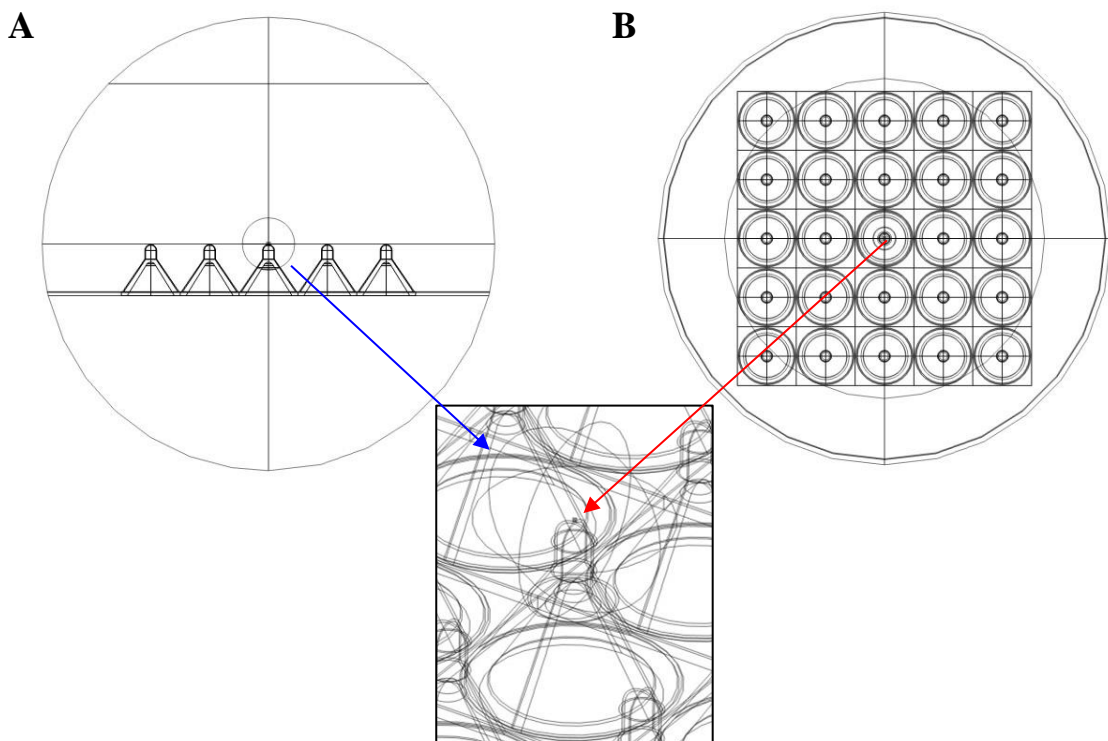

Figure 18 - Scheme of the 5x5 model. (A) Side projection. (B) Top projection. Explanatory insert with a detailed image of the central element of the array and the location of the electric dipole

In addition to the location of the dipole, the orientation of the dipole is also an important factor. The orientation of the dipole also affects the direction and

magnitude of the photoluminescence. During the modeling, the three main polarizations of the electrical dipole p_x, p_y, p_z will be considered. Radiation patterns and photoluminescence spectra will be averaged over the main polarizations of the electric dipole (p_x, p_y, p_z). Another important factor that must also be taken into account when modeling photoluminescence is the probability of emitting a photon at a certain wavelength, that is, the spectral dependence of the photoluminescence of HgTe quantum dots. When simulating the emission of quantum dots, the spectral characteristic of the photoluminescence of HgTe quantum dots in solution, obtained experimentally (Figure 19), will be used. This spectral characteristic will be related to the amplitude of the electric dipole field as the square root of the experimental intensity, since it is known that $I \propto E^2$.
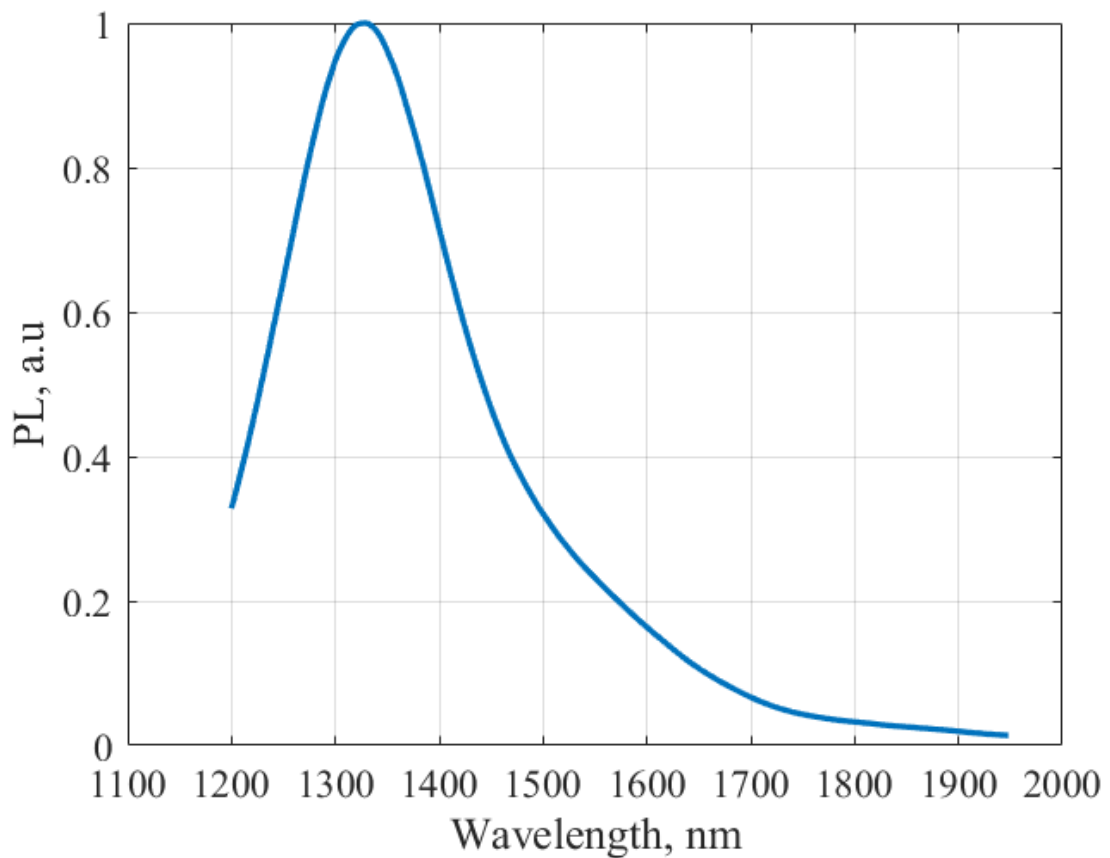

Figure 19 - Spectral dependence of photoluminescence of HgTe quantum dots in solution

3. Results and discussion

3.1 Eigenfrequency analysis

Let us fix the geometric parameters of the structure (period of structure Λ=1000 nm, spacer thickness d=20 nm, height of jet h=250 nm) and find the high-Q eigenmodes of the metasurface depending on the Bloch vector in the Brillouin G-X zone (Figure 20).
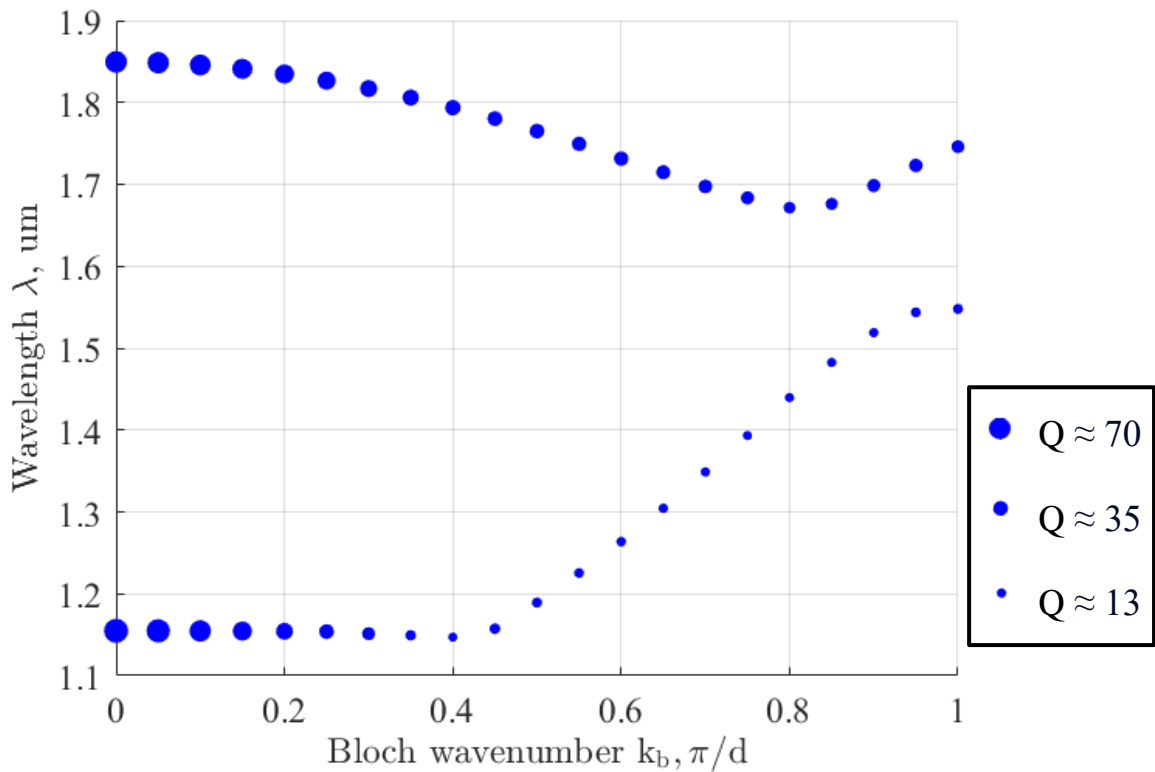

Figure 20 - Dispersion of plasmon modes supported by the metasurface in the Γ-X section of the Brillouin zone. The size of the filled circle is proportional to the Q-factor of mode (Λ=1000 nm, d=20 nm, h=250 nm)

The largest clusters reach the Q-factor of 75. As the value of the Bloch vector increases, the Q-factor of mode decreases to 13–15 (the smallest sizes). The corresponding field distributions at the Γ point for the upper and lower branches are shown in Figure 21 (A) and Figure 21 (B) respectively.
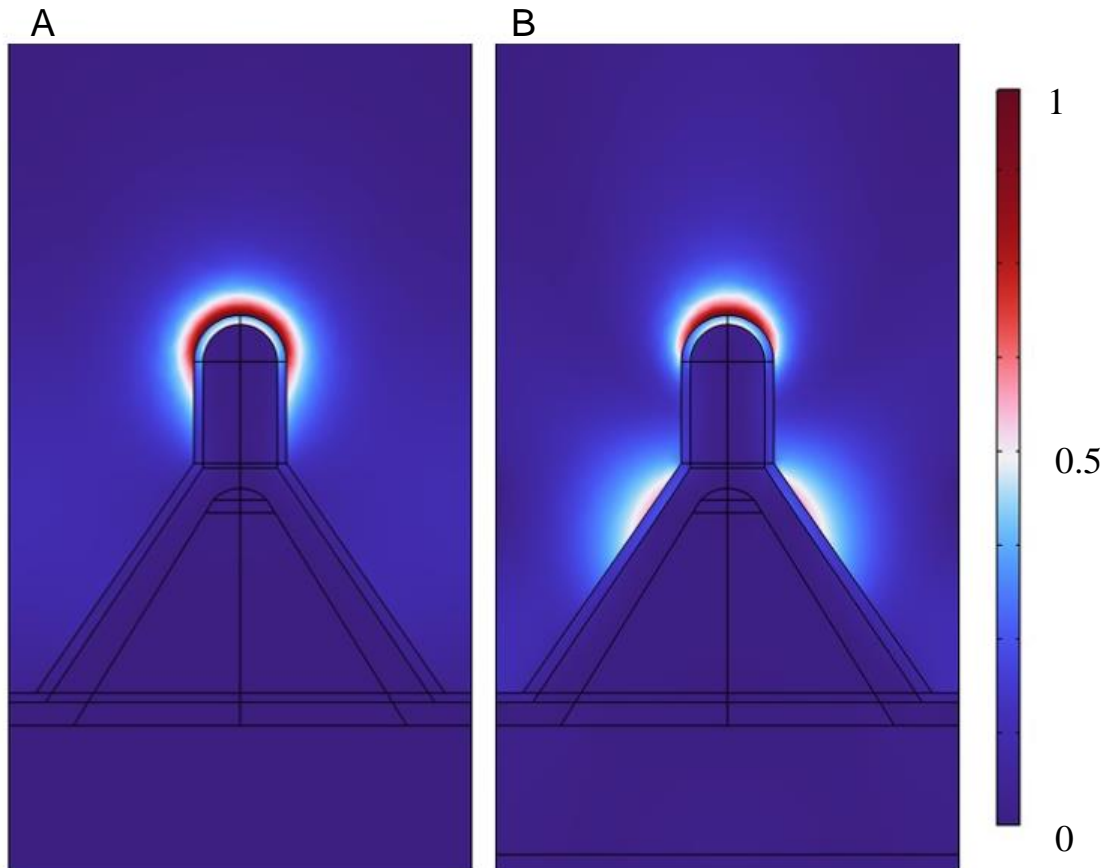

Figure 21 - (A) Electric field distribution of the upper branch ($\lambda_R > \Lambda$). (B) Electric field distribution of the lower branch ($\lambda_R \cong \Lambda$)

As we can see, both modes are characterized by extremely high localization of the field at the jet tip. The only difference is the presence of a nonzero electric field on the outer walls of the cone for mode (B). Systematic calculation showed that both modes are sensitive to the array period Λ and the spacer thickness; however, only the second one ($\lambda_R > \Lambda$) appeared to be sensitivity to the variation of the nanojet height. This mode plays the key role in the enhancement of PL emission and FTIR reflection spectrum. To produce a more detailed analysis for the eigenmode $\lambda R > \Lambda$, one can obtain the following map of the dependence of the position along the

wavelength of the eigenmode on the height of the jet and the period of the plasmon metasurface (Fig.22)
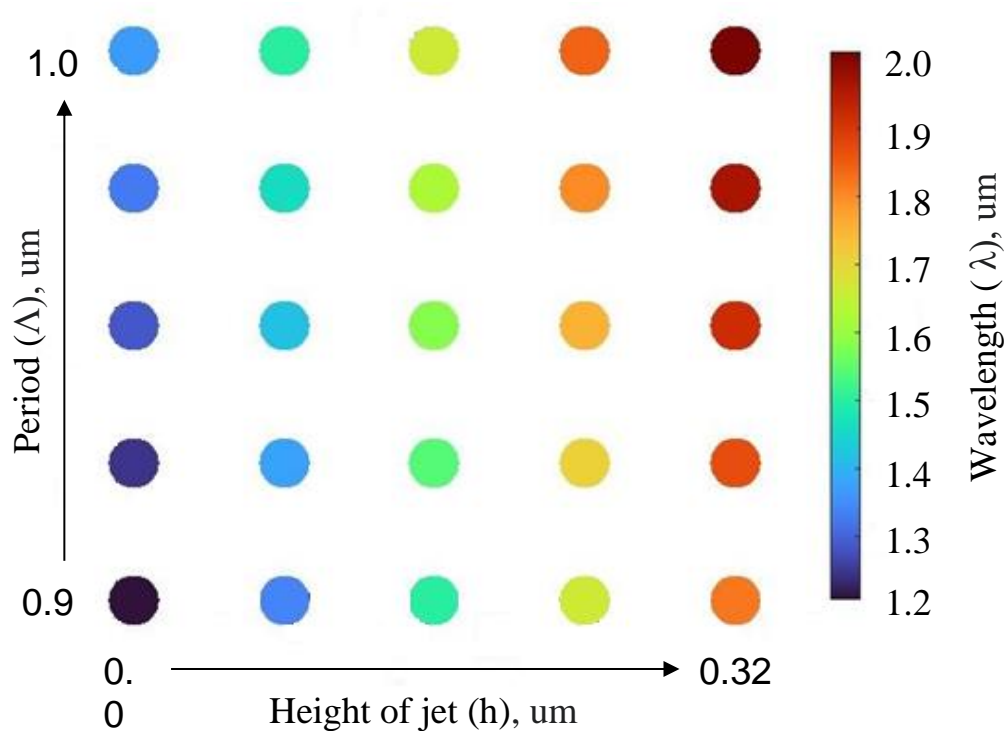

Figure 22 - Dependence of plasmon modes wavelengths on period of structure and height of jet at the Γ-point of the Brillouin zone. The color of the filled circle is a wavelength of plasmon mode

Based on these results, we can control the position of the plasmon mode in a linear manner in the wavelength range from 1 to 2 um. In this case, the field distribution does not change and looks like in Figure 21 (A).

3.2 Reflectance spectra

Let us consider the excitation of a plasmonic metasurface by a plane wave front of TM polarization. In particular, let us take the geometry of the structure with the parameters: spacer thickness = 10 nm, height of jet = 10 nm, period = 900 nm, and the position of the eigenmode at the Γ point at a wavelength of 1172 nm. Let us plot a reflection map for such a geometry depending on the wavelength and angle of

incidence, and the angle of incidence will change in a small range from 0 ° to 8 ° with a step of 30', and the wavelength varies in the range from 1115 nm to 1220 nm with a step of 2.5 nm (Figure 23). As we see from the reflection spectrum, the mode cannot be excited at a strictly normal incidence. Since mode is BIC. With a slight increase in the angle of incidence, a dip appears in the reflection spectrum. Moreover, a dip in the reflectance spectrum appears drastically, beyond 2° the reflectance drops by 40-50%. More details about the BIC mode will be described in the next paragraph.
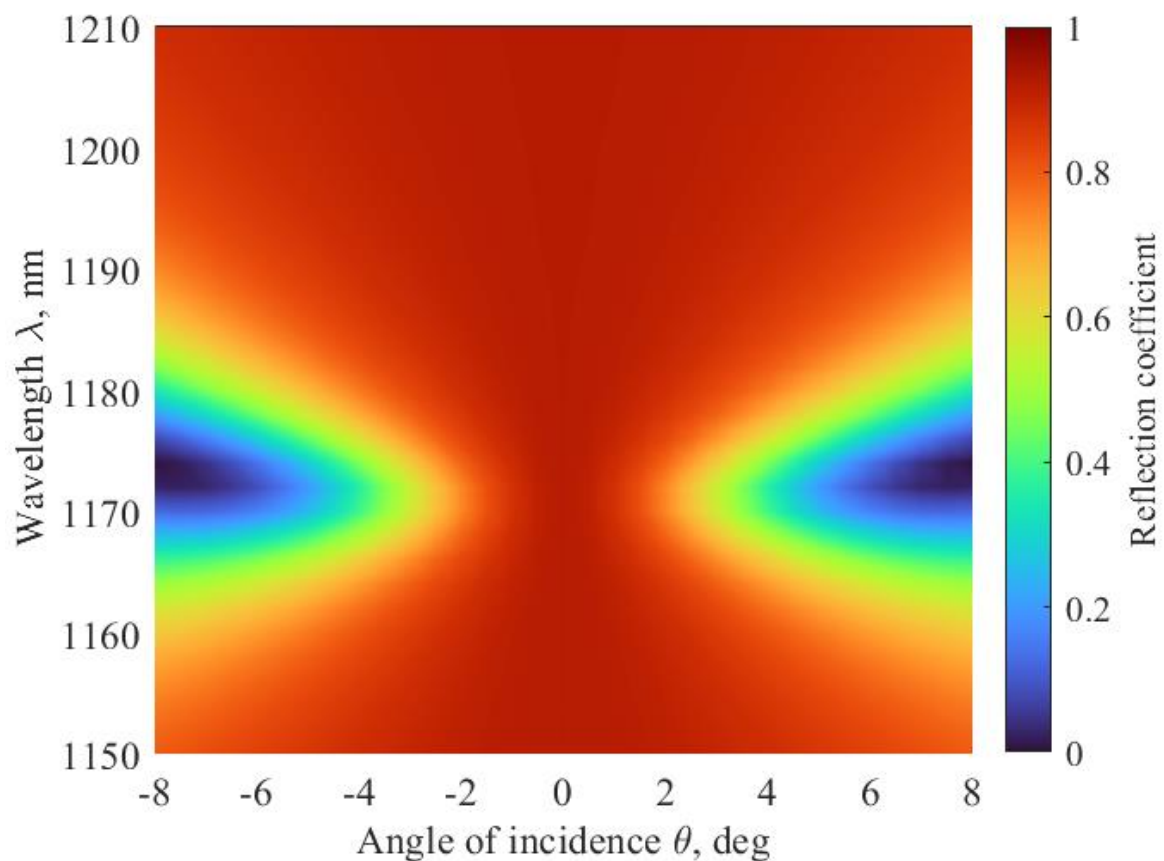

Figure 23 - Calculated reflection spectrum of the metasurface (spacer thickness is 10 nm, Λ= 900 nm, height of jet is 10 nm) as a function of incidence angle θ of the excited plane wave

Next, we will produce a series of simulations with a plane wave incidence of the TM polarization but with a small and fixed angle of 5°. Check which parameters affect the position of the decline in the reflection spectrum (Figure 24) and how they do so. The position of the dip (Figure 24 (circles)) in the reflection spectrum shifts

towards longer wavelengths with increasing period/jet height/spacer thickness Al_2O_3. Fitting demonstrates that the position of the dip in the reflection spectrum is linearly dependent on the geometric parameters of the metasurface. The data obtained are in complete agreement with the eigenmode analysis from the previous section.
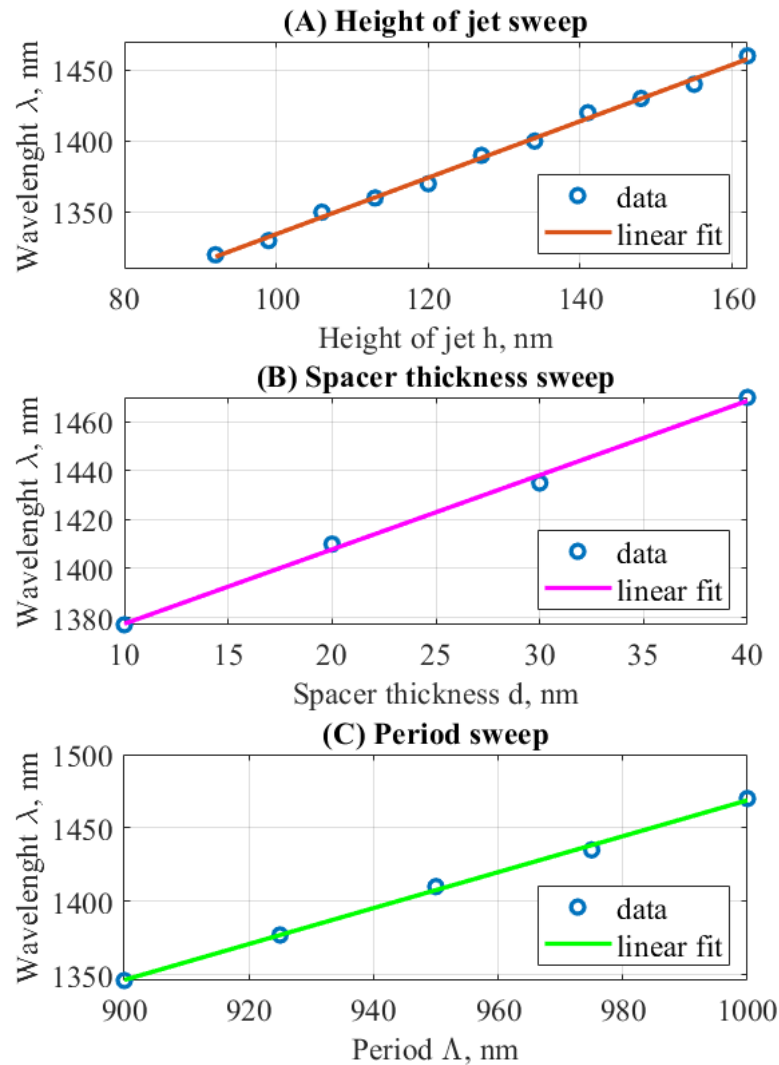

Figure 24 - (A) Dependence of the position of the dip on the height of jet. (B) Dependence of the position of the dip on the spacer thickness Al_2O_3. (C) Dependence of the position of the dip on the period

For similar structure geometries, we can compare the reflection spectra obtained experimentally and numerically (Figure 25).
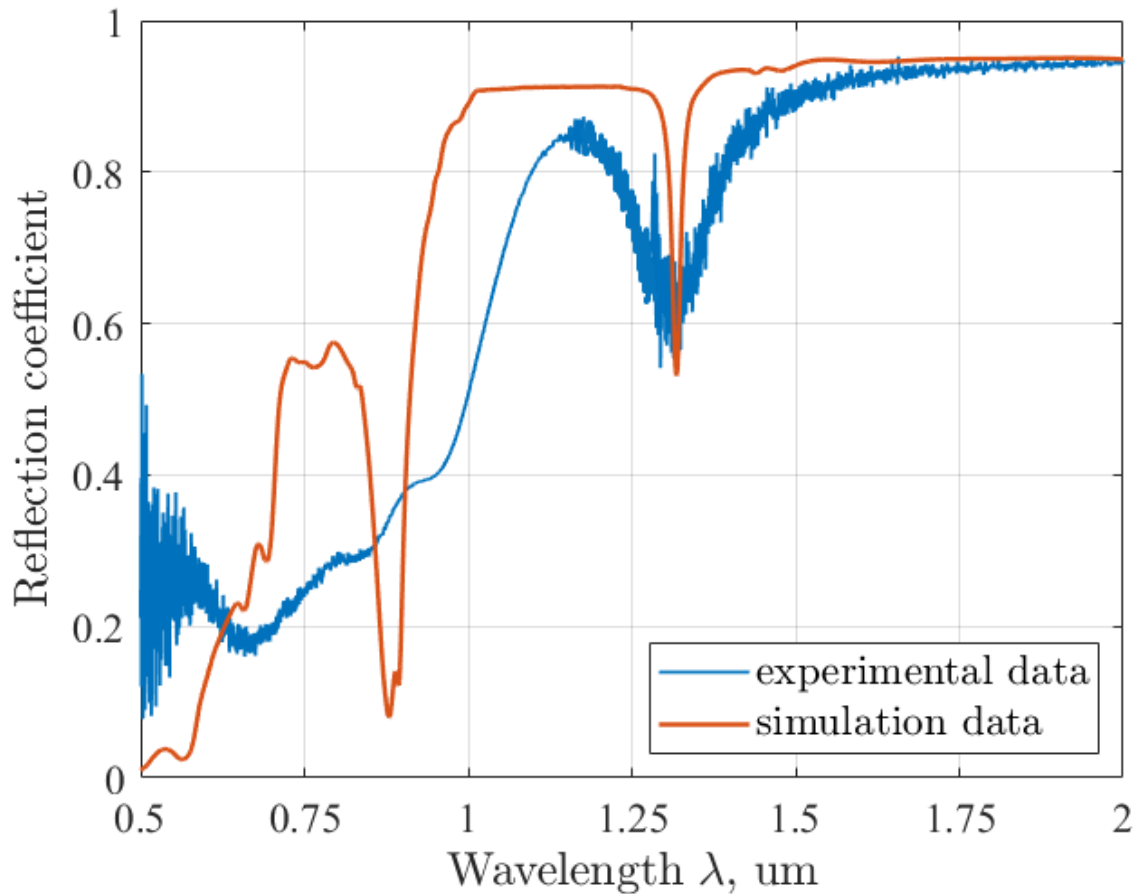
Figure 25 - Reflectance spectra. Blue line - experimental data. Red line - simulation data. Period $\Lambda = 900$ nm, spacer thickness Al_2O_3 d= 10 nm, height of jet h= 92 nm

As seen on the graph, the mode $\lambda_R > \Lambda$ coincides in the position of the dip both in the experiment and in the simulation, but the width of the dip is different. The dip in the experiment is much wider, which can be explained by the inhomogeneous thickness of the metal and sensibility to roughness of the structure. The $\lambda_R \cong \Lambda$ mode is observed during simulation, but in the experiment, it is practically indistinguishable in the measured reflection spectrum, apparently due to increased ohmic losses closer to the visible region of the spectrum, as well as spectral overlap with multiple high-order resonances located there.

It is important to note that in the experiment it is possible to detect the mode at normal incidence, but not in numerical simulation. This is because in experiment

small apertures are used for simulation of a plane wave. Therefore, when we say that in the experiment a plane wave falls normally on the structure, in fact, such radiation will be slightly collimated. As we have already shown, even a small value of the angle of incidence leads to excitation of the mode. This is exactly what happens in the experiment.

3.3 qBIC

In (Figure 23), a map of the reflection spectrum versus wavelength λ and angle of incidence θ was shown. As we noted in section 3.2, it is not possible to excite a mode at strictly normal incidence. However, in Section 3.1, the mode can be detected both at the Γ point and in the entire Γ-X zone. The reason for this behavior is that the qBIC. This can be proven in several ways.

First, this can be shown from the distribution of the electric field components [51]. Consequently, if we consider in detail the electric field components in the analysis for eigenmodes (Figure 26), we will observe that the electric field components are distributed in an odd way which makes the mode "dark" for normal plane wave excitation.
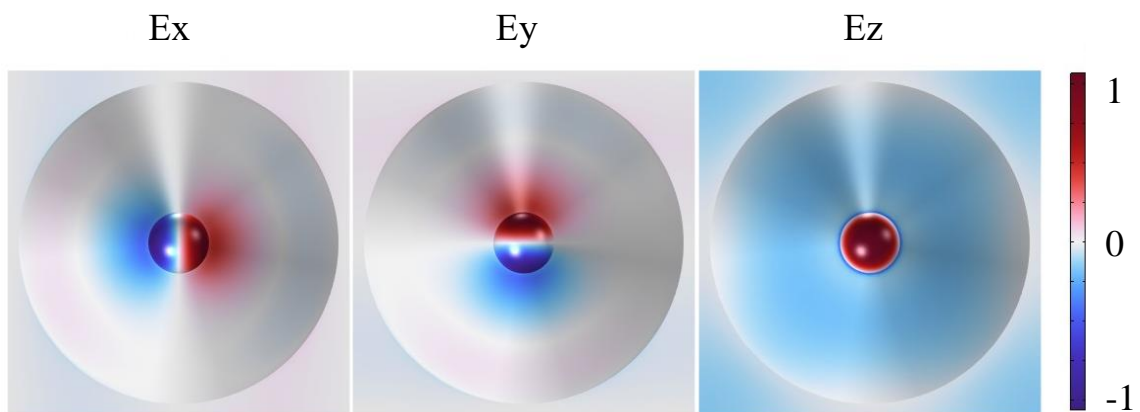

Figure 26 - Electric field distribution Ex, Ey, Ez. (Normalized). Top view

The second way is to calculate the radiative and non-radiative Q-factors in the Brillouin Γ-X zone. By numerically counting the energy absorbed by the metal and dividing by the total mode energy, we can obtain γ_{nr}. Similarly, one can find the

energy flowing out of the ends of the cell and divide by the total energy of the system to find γ_r. Accordingly, the quality factor can be found as $Q = \dfrac{\Omega}{2\gamma}$, and then the total quality factor of the system will be equal to

$$\frac{1}{Q_{total}} = \frac{1}{Q_r} + \frac{1}{Q_{nr}}.\qquad(1)$$

Based on this, we plotted a graph on a semi-logarithmic scale in the Brillouin zone Γ-X (Figure 27). As shown, as the radiation Q-factor approaches the Γ point, it increases dramatically and reaches 10^7. With an increase in mesh density, the radiation factor will increase by several orders of magnitude. In fact, the radiation quality factor tends to infinity. The finite quality factor is obtained due to the fact that the mesh element sizes are finite. The total quality factor does not tend to infinity, since there are always losses in the system, especially in a system with metal. However, qBIC contributes to an increase in the total quality factor as one approaches the Γ point. The graph is plotted for the mode λ_R>Λ, however, for the mode $\lambda_R \cong \Lambda$ the mechanism for increasing the radiation quality factor near the Γ point is similar. Based on the proof presented above, we can conclude that both modes are qBIC.
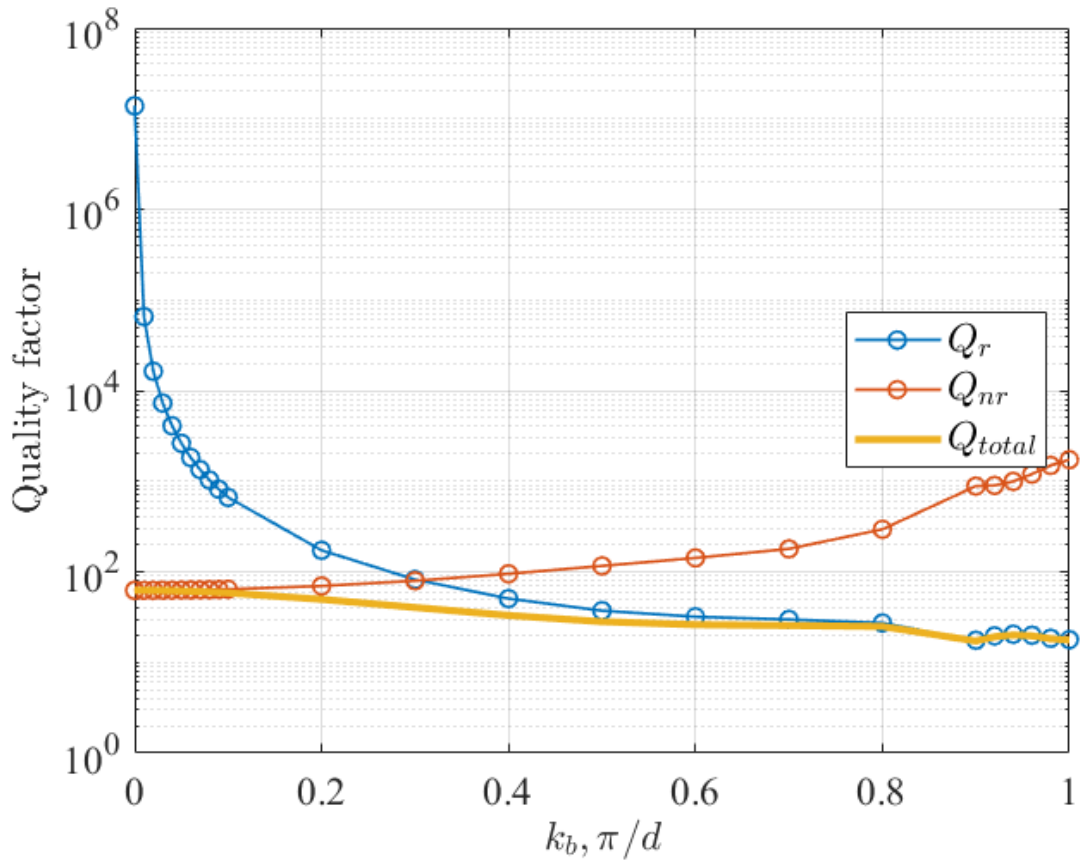
Figure 27 - Calculated Brillouin zone dependence of radiative Q_{rad}, nonradiative Q_{nr}, and total Q_{tot} quality factors of the qBIC

3.4 Photoluminescence

After the detection of the corresponding plasmonic modes. It is possible to combine the photoluminescence of HgTe quantum dots with the plasmon mode. First, let's turn to the results of the experiment (Figure 28).
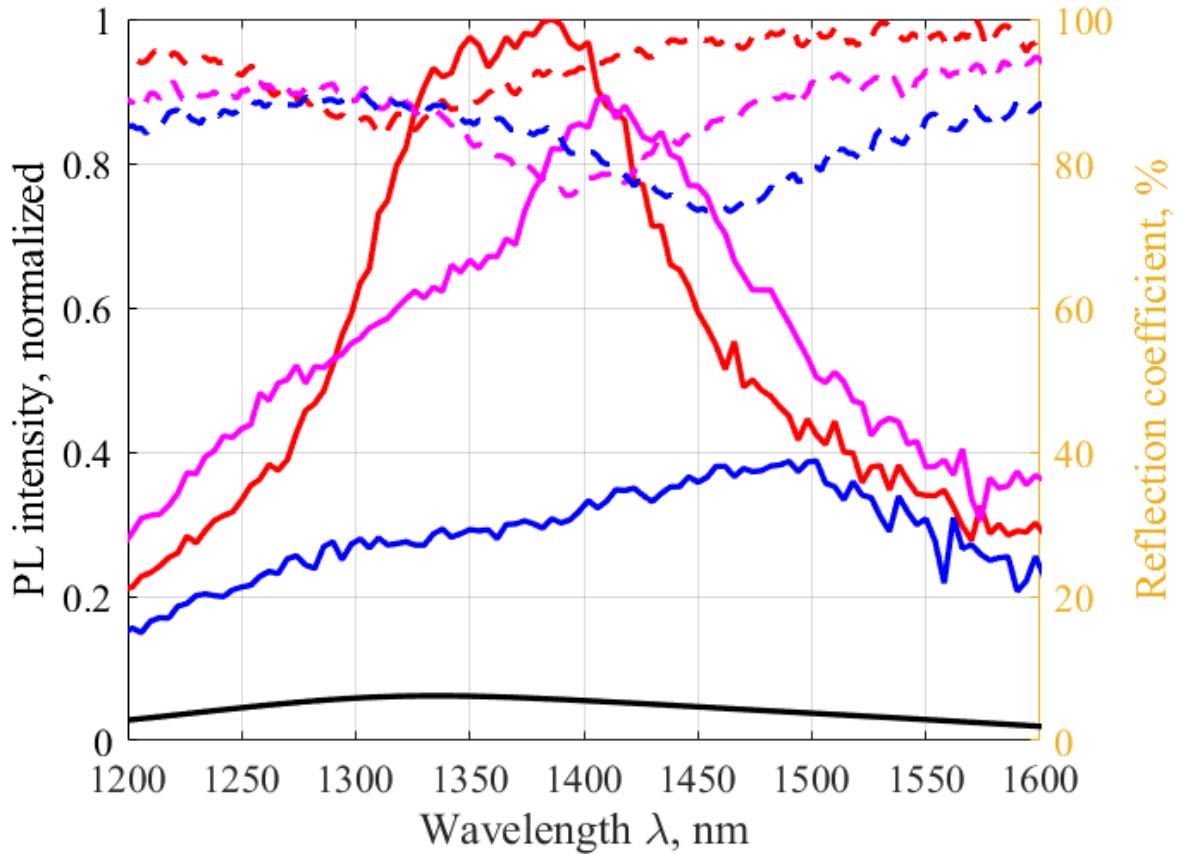
Figure 28 - Dashed lines - reflection spectrum. Solid line - PL spectrum. Red - height of jet ≈ 90 nm, purple - height of jet ≈ 130 nm, blue - height of jet ≈ 160 nm. Black solid line - reference spectrum of QD in solution. Period Λ = 900 nm, Spacer thickness Al_2O_3 d = 10 nm

The equality $\lambda_{PL} = \lambda_R = 1320$ nm (λ_{PL} is the photoluminescence wavelength, λ_R is the plasmon mode wavelength) corresponds to the red color ((photoluminescence is maximum). Further, as the jet height increases, the dip in the reflection spectrum shifts towards longer wavelengths and, accordingly, the plasmon mode shifts. However, the photoluminescence of quantum dots (black line) decreases with increasing wavelength. Accordingly, we observe a decrease in photoluminescence (purple and blue lines).

We can simulate this effect. We know how the position of the dip depends on the geometric parameters, so we can easily select such parameters at which the position of the mode along the wavelength will coincide with the maximum of the photoluminescence spectrum of quantum dots, in particular $\lambda_{PL} = \lambda_R = 1320$ nm. Once

again, we note that the mode $\lambda_R \cong \Lambda$ is not sensitive to changes in the jet height, so we also work here with the mode $\lambda_R > \Lambda$. Based on the localization of the plasmon mode field, we place a point electric dipole on the upper point of the jet at the height of the quantum dot monolayer (4 nm). And we can plot a photoluminescence spectrum (Figure 29) for three structures, which have different jet heights, and hence the position of the plasmon mode. As we see from the figure, the maximum photoluminescence (red line) also corresponds to the case of a jet height of 92 nm. The plasmon mode also shifts with increasing jet height. However, the photoluminescence of quantum dots is fixed, therefore, after $\lambda_{PL} = 1320$ nm the emission of quantum dots decreases (black line) and, as a result, the photoluminescence of the plasmonic metasurface decreases (purple and blue lines). According to the position of the dip in the reflection spectrum and the photoluminescence maximum, there is a correspondence with the experimental data. However, the photoluminescence width in the experiment is larger. This is due to the fact that the width of the dips in the reflection spectrum is wide, and this is due to the variable thickness of gold in the microbumps [52].
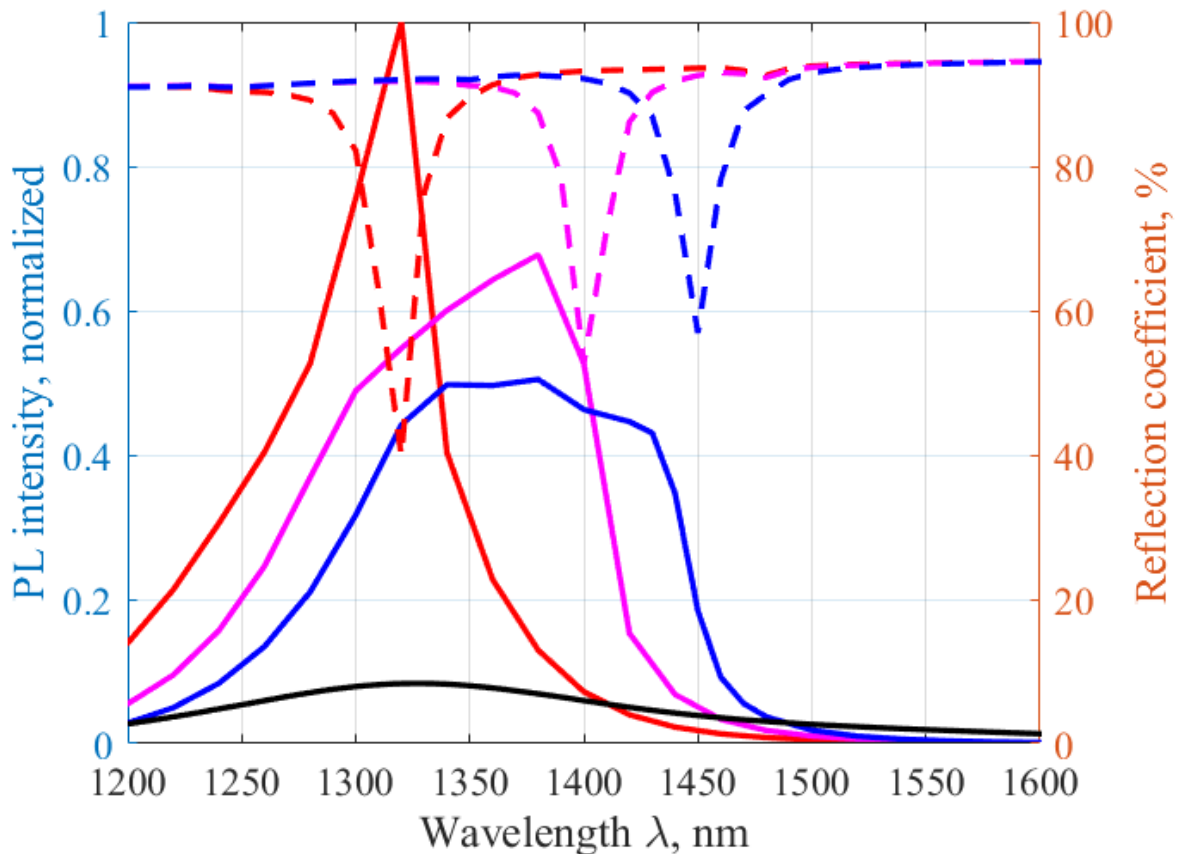
A logical continuation of the study of photoluminescence on plasmonic metasurfaces is the calculation of the Purcell effect. Systematic modeling, as well as experimental results, shows that the maximum possible enhancement in photoluminescence is 12 (Figure 30). In experiment, it is possible to apply layers with a thickness multiple of 10 nm. However, in numerical simulations, we are not limited to this. Therefore, additional points are presented on the graph.
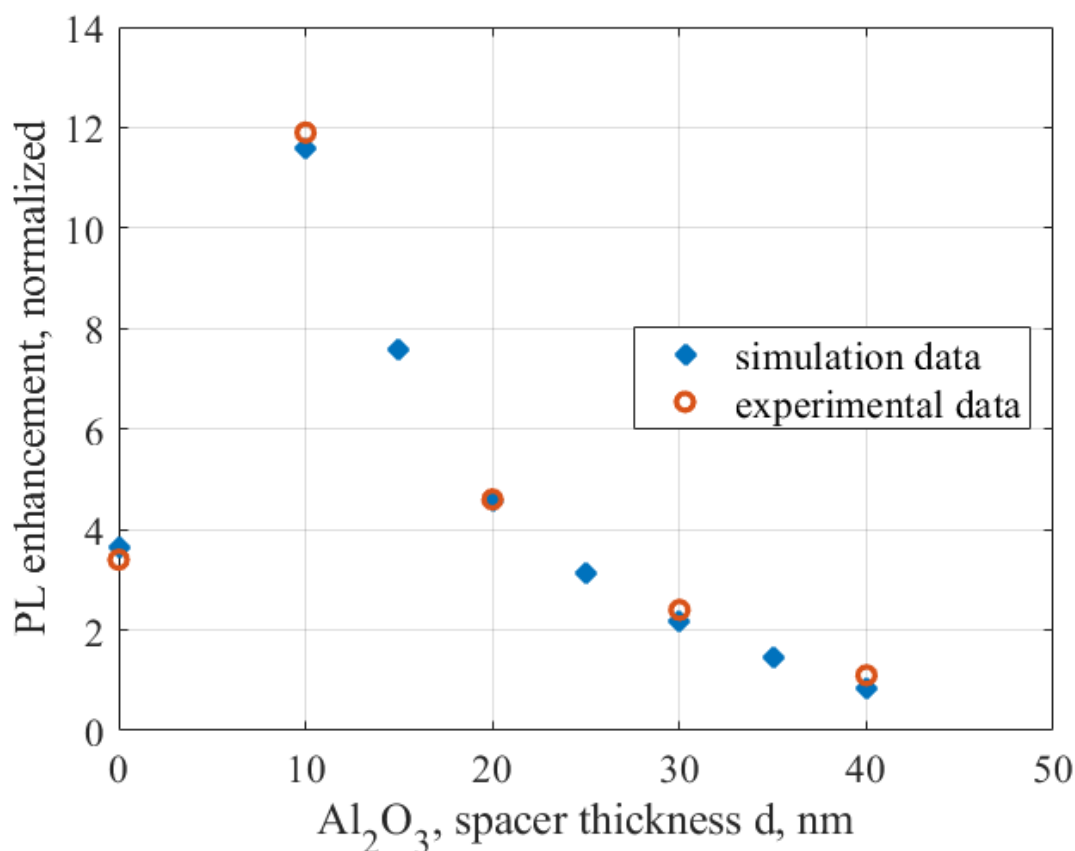

Figure 30 - PL enhancement dependence on spacer thickness Al_2O_3. Normalization to the surface without mirobumps. Height of jet = 92 nm, period Λ = 900 nm

The normalized photoluminescence (PL) of the quantum dot (QD) monolayer was analyzed in Figure 30, where the red circles depict the results. The data shows

that the spontaneous emission is over ten times stronger at an optimal spacer thickness of d=10 nm. The empirical observations are in complete concurrence with the outcomes of the computational models depicted in Figure 30 featuring the gray circles. Finite arrays were employed in the simulations utilizing point dipole sources. Additionally, we examined the impact of spectral detuning between the BIC and the QD emission maximum on the PL yield. The fabricated metasurface, which exhibited a varied nanobump geometry, demonstrated a red shift in resonance as the height of the nanobumps increased.

3.5 Far-field

In addition to the integral characteristics of photoluminescence, it is also useful to discuss the angular distributions of energy fluxes in this process, since the result of the experiment can strongly depend on such a distribution. Let's plot a radiation pattern (Figure 31). The radiation is not axisymmetric in φ, so we also averaged the radiation pattern over φ. As we can see, the radiation goes mainly in angles from 14° to 35° degrees.

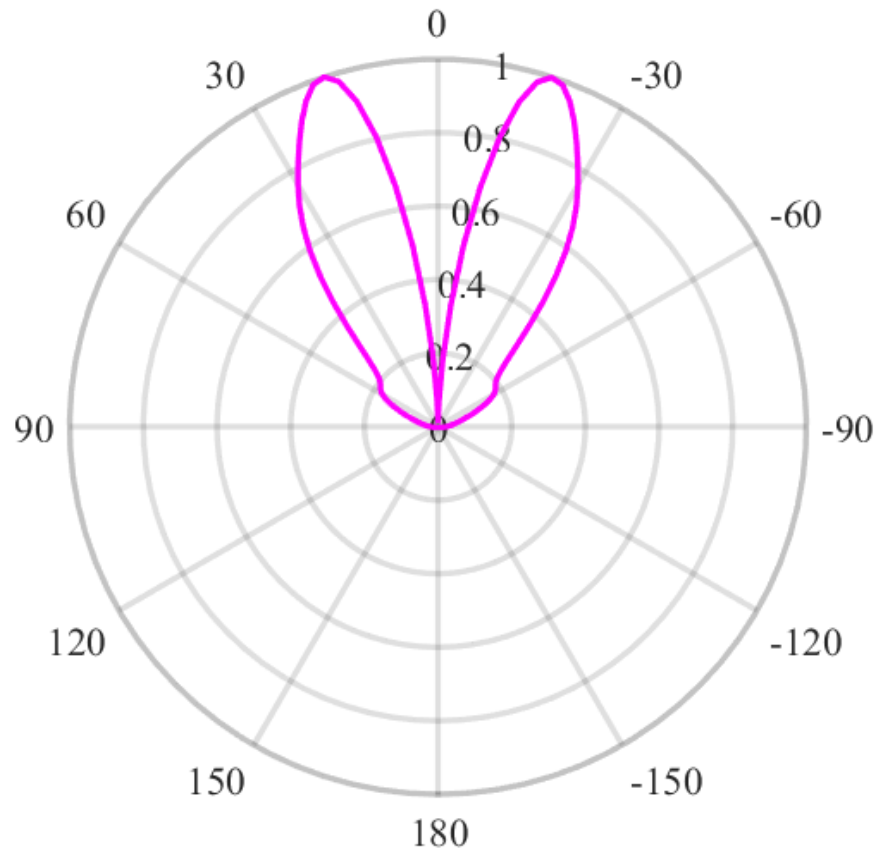Figure 31 - Far-Field Radiation Pattern. Intensity is normalized. Period $\Lambda = 900$ nm, Al_2O_3 spacer thickness $= 10$ nm, height of jet $= 92$ nm

In the experiment, the value of photoluminescence was measured for objectives with different numerical apertures. Accordingly, it is possible to integrate the radiation pattern (Figure 31) over the angles and compare the result with the experiment.
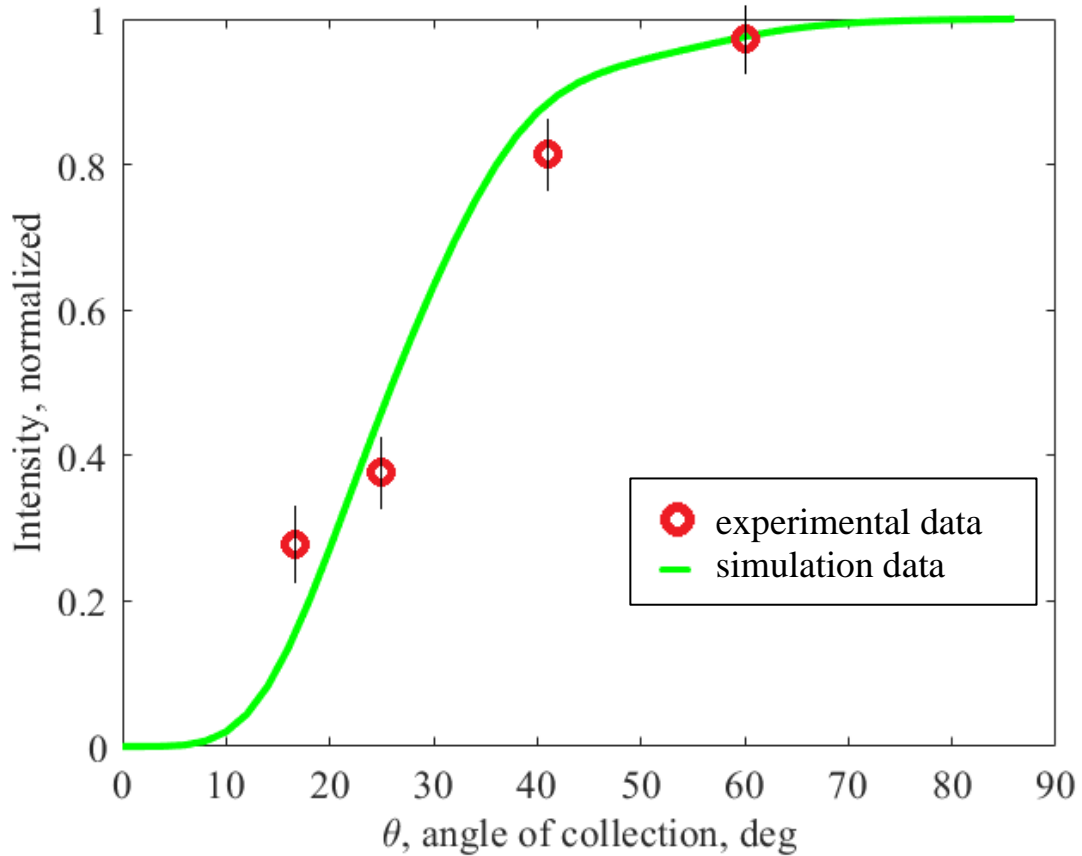
Figure 32 - Calculated (solid curve) and measured (dots) normalized PL intensity as a function of the collection angle θ. Period **Λ** = 900 nm, Al_2O_3 spacer thickness = 10 nm, height of jet = 92 nm

The integral characteristic is shown in (Figure 32). Red dots correspond to the experimental values measured using objectives with numerical aperture NA=0.25, NA=0.4, NA=0.65, NA=0.85. As can be seen from the graph, after 40°, the graph reaches saturation and further expansion weakens. According to the nature of BIC mode the radiation in the direction normal to the surface is suppressed that is confirmed by the simulation results (Figures 31,32).

3.6 Localized surface plasmon resonance of the isolated nanojet

To shed more light onto the origin of the observed BIC modes in the plasmonic metasurface, it is very illustrative to consider the modes supported by the

isolated nanostructures. For such simulations, we analyzed the localized surface plasmon resonant (LSPR) modes of the isolated nanojet placed on the glass substrate, while the smooth parts of the Au film were removed, and the simulation volume was limited by PML boundary conditions. Performed simulations (Figure 33) revealed close similarity between structure of the EM fields of the BIC mode supported by an array of identical nanojets and LSPR of the isolated nanojet with the same geometry. The only difference is that the LSPR position is spectral shifted towards larger wavelengths (1570 nm) with respect to qBIC mode (1320 nm) due to collective lattice interaction between the bumps.
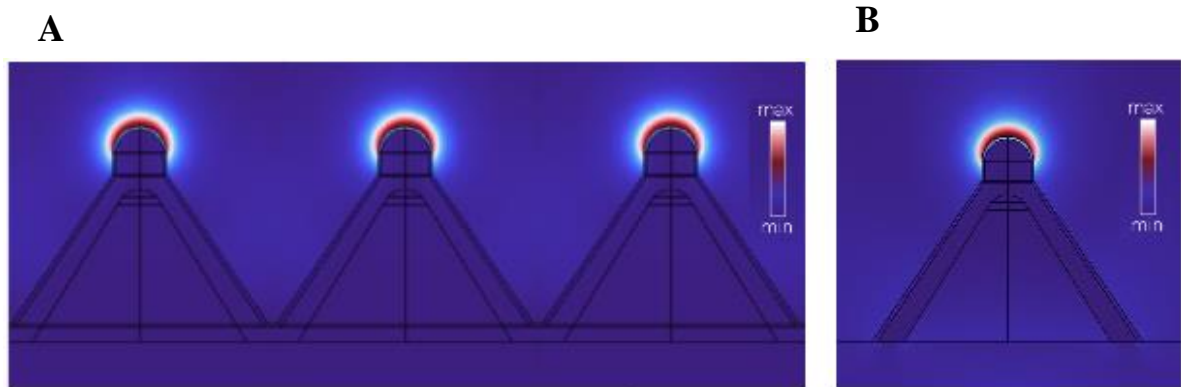

Figure 33 - EM-field amplitude calculated for nanojet array (Λ=900 nm, d=10 nm, h=92 nm; left panel) and isolated nanojets of the same size placed on the glass substrate. The corresponding wavelength of collective BIC mode and localized surface plasmon resonance of the isolated structure are 1320 and 1570 nm, respectively

CONCLUSION

The simulation results assisted to explain the experiment data. It was shown that plasmon mode in the IR range linearly depends on geometric parameters of structure: the height of the jet h, the spacer thickness Al_2O_3, period **Λ**. Moreover, it has been proven that the plasmonic mode supported by the metasurface in the IR range is qBIC, due to which the Q-factor of the mode reaches 70-80. The finite array modeling method quantitatively and qualitatively explains the behavior of metasurface photoluminescence. As shown by numerical simulation and experiment, the optimal thickness of the Al_2O_3 spacer is d=10 nm. It follows from the far-field radiation pattern that the plasmonic metasurface emits predominantly in the range of angles from 15° to 35°, the maximum photoluminescence is reached at 17°. In fact, the mode is also observed for a single microbump, however, due to the absence of collective grating effects, the mode is shifted towards longer wavelengths. The proposed approach, which utilizes cost-effective and easily scalable direct fs-laser printing to fabricate the qBIC supporting metasurface, has the potential to pave the way for the development of advanced near-IR-light emitting devices and photodetectors in the future.

REFERENCES

1.   Qu J. et al. Electroluminescence from Nanocrystals above 2 μm //Nature Photonics. – 2022. – T. 16. – №. 1. – C. 38-44.

2.   Dai L. et al. Conjugated polymers for light-emitting applications //Advanced Materials. – 2001. – T. 13. – №. 12-13. – C. 915-925.

3.   Trofymchuk K. et al. Addressable nanoantennas with cleared hotspots for single-molecule detection on a portable smartphone microscope //Nature communications. – 2021. – T. 12. – №. 1. – C. 950.

4.   Shiohara A., Wang Y., Liz-Marzán L. M. Recent approaches toward creation of hot spots for SERS detection //Journal of Photochemistry and Photobiology C: Photochemistry Reviews. – 2014. – T. 21. – C. 2-25.

5.   Punj D. et al. A plasmonic 'antenna-in-box'platform for enhanced single-molecule analysis at micromolar concentrations //Nature nanotechnology. – 2013. – T. 8. – №. 7. – C. 512-516.

6.   Benz F. et al. Single-molecule optomechanics in "picocavities" //Science. – 2016. – T. 354. – №. 6313. – C. 726-729.

7.   Chikkaraddy R. et al. Single-molecule strong coupling at room temperature in plasmonic nanocavities //Nature. – 2016. – T. 535. – №. 7610. – C. 127-130.

8.   Tserkezis C. et al. Hybridization of plasmonic antenna and cavity modes: Extreme optics of nanoparticle-on-mirror nanogaps //Physical Review A. – 2015. – T. 92. – №. 5. – C. 053811.

9.   Akselrod G. M. et al. Probing the mechanisms of large Purcell enhancement in plasmonic nanoantennas //Nature Photonics. – 2014. – T. 8. – №. 11. – C. 835-840.

10.   Raza S. et al. Multipole plasmons and their disappearance in few-nanometre silver nanoparticles //Nature communications. – 2015. – T. 6. – №. 1. – C. 8788.

11. Takata H. et al. Detailed observation of multiphoton emission enhancement from a single colloidal quantum dot using a silver-coated AFM tip //Nano Letters. – 2016. – T. 16. – №. 9. – C. 5770-5778.

12. Khatua S. et al. Resonant plasmonic enhancement of single-molecule fluorescence by individual gold nanorods //ACS nano. – 2014. – T. 8. – №. 5. – C. 4440-4449.

13. Abadeer N. S. et al. Distance and plasmon wavelength dependent fluorescence of molecules bound to silica-coated gold nanorods //ACS nano. – 2014. – T. 8. – №. 8. – C. 8392-8406.

14. Punj D. et al. Self-assembled nanoparticle dimer antennas for plasmonic-enhanced single-molecule fluorescence detection at micromolar concentrations //ACS photonics. – 2015. – T. 2. – №. 8. – C. 1099-1107.

15. Puchkova A. et al. DNA origami nanoantennas with over 5000-fold fluorescence enhancement and single-molecule detection at 25 μM //Nano letters. – 2015. – T. 15. – №. 12. – C. 8354-8359.

16. Lim D. K. et al. Highly uniform and reproducible surface-enhanced Raman scattering from DNA-tailorable nanoparticles with 1-nm interior gap //Nature nanotechnology. – 2011. – T. 6. – №. 7. – C. 452-460.

17. Ayala-Orozco C. et al. Fluorescence enhancement of molecules inside a gold nanomatryoshka //Nano letters. – 2014. – T. 14. – №. 5. – C. 2926-2933.

18. Park J. E. et al. Highly controlled synthesis and super-radiant photoluminescence of plasmonic cube-in-cube nanoparticles //Nano letters. – 2016. – T. 16. – №. 12. – C. 7962-7967.

19. Nam J. M. et al. Plasmonic nanogap-enhanced Raman scattering with nanoparticles //Accounts of chemical research. – 2016. – T. 49. – №. 12. – C. 2746-2755.

20. Zhang T. et al. Optimally designed nanoshell and matryoshka-nanoshell as a plasmonic-enhanced fluorescence probe //The Journal of Physical Chemistry C. – 2012. – T. 116. – №. 15. – C. 8804-8812.

21. Theodorou I. G. et al. Significant metal enhanced fluorescence of Ag 2 S quantum dots in the second near-infrared window //Nanoscale. – 2016. – T. 8. – №. 26. – C. 12869-12873.

22. Walling M. A., Novak J. A., Shepard J. R. E. Quantum dots for live cell and in vivo imaging //International journal of molecular sciences. – 2009. – T. 10. – №. 2. – C. 441-491.

23. Kovalenko M. V. et al. SnTe nanocrystals: a new example of narrow-gap semiconductor quantum dots //Journal of the American Chemical Society. – 2007. – T. 129. – №. 37. – C. 11354-11355.

24. Keuleyan S., Lhuillier E., Guyot-Sionnest P. Synthesis of colloidal HgTe quantum dots for narrow mid-IR emission and detection //Journal of the American Chemical Society. – 2011. – T. 133. – №. 41. – C. 16422-16424.

25. Kravets V. G. et al. Plasmonic surface lattice resonances: a review of properties and applications //Chemical reviews. – 2018. – T. 118. – №. 12. – C. 5912-5951.

26. Bin-Alam M. S. et al. Ultra-high-Q resonances in plasmonic metasurfaces //Nature communications. – 2021. – T. 12. – №. 1. – C. 974.

27. Sugai S. et al. Comparison of the soft modes in tantalum dichalcogenides //Physica B+ C. – 1981. – T. 105. – №. 1-3. – C. 405-409.

28. Bogdanov A. A. et al. Bound states in the continuum and Fano resonances in the strong mode coupling regime //Advanced Photonics. – 2019. – T. 1. – №. 1. – C. 016001-016001.

29. Neubrech F. et al. Surface-enhanced infrared spectroscopy using resonant nanoantennas //Chemical reviews. – 2017. – T. 117. – №. 7. – C. 5110-5145.

30. Ye W. et al. Plasmonic nanostructures in solar energy conversion //Journal of Materials Chemistry C. – 2017. – T. 5. – №. 5. – C. 1008-1021.

31. Seo I. C. et al. Circularly polarized emission from organic–inorganic hybrid perovskites via chiral fano resonances //ACS nano. – 2021. – T. 15. – №. 8. – C. 13781-13793.

32.	Ra'di Y., Krasnok A., Alú A. Virtual critical coupling //ACS Photonics. – 2020. – Т. 7. – №. 6. – С. 1468-1475.

33.	Koshelev K., Bogdanov A., Kivshar Y. Meta-optics and bound states in the continuum //Science Bulletin. – 2019. – Т. 64. – №. 12. – С. 836-842.

34.	Liang Y. et al. Hybrid anisotropic plasmonic metasurfaces with multiple resonances of focused light beams //Nano Letters. – 2021. – Т. 21. – №. 20. – С. 8917-8923.

35.	Aigner A. et al. Plasmonic bound states in the continuum to tailor light-matter coupling //Science Advances. – 2022. – Т. 8. – №. 49. – С. eadd4816.

36.	Laux F., Bonod N., Gérard D. Single emitter fluorescence enhancement with surface lattice resonances //The Journal of Physical Chemistry C. – 2017. – Т. 121. – №. 24. – С. 13280-13289

37.	Landau L. D. et al. Electrodynamics of continuous media. – elsevier, 2013. – Т. 8.

38.	Vaskin A. et al. Light-emitting metasurfaces //Nanophotonics. – 2019. – Т. 8. – №. 7. – С. 1151-1198.

39.	Yang Y. et al. All-dielectric metasurface analogue of electromagnetically induced transparency //Nature communications. – 2014. – Т. 5. – №. 1. – С. 5753.

40.	Stankevičius E. et al. Direct Laser Writing for the Formation of Large-Scale Gold Microbumps Arrays Generating Hybrid Lattice Plasmon Polaritons in Vis–NIR Range //Advanced Optical Materials. – 2021. – Т. 9. – №. 12. – С. 2100027.

41.	Shepelev V. V. et al. Action of a femtosecond laser pulse on thin metal film supported by glass substrate //Journal of Physics: Conference Series. – IOP Publishing, 2018. – Т. 1128. – №. 1. – С. 012092.

42.	Meshcheryakov Y. P., Bulgakova N. M. Thermoelastic modeling of microbump and nanojet formation on nanosize gold films under femtosecond laser irradiation //Applied Physics A. – 2006. – Т. 82. – С. 363-368.

43. Stankevičius E. et al. Engineering electrochemical sensors using nanosecond laser treatment of thin gold film on ITO glass //Electrochimica Acta. – 2019. – T. 297. – C. 511-522.

44. Pavlov D. et al. Tuning Collective Plasmon Resonances of Femtosecond Laser-Printed Metasurface //Materials. – 2022. – T. 15. – №. 5. – C. 1834.

45. Pavlov D. et al. 10-million-elements-per-second printing of infrared-resonant plasmonic arrays by multiplexed laser pulses //Optics letters. – 2019. – T. 44. – №. 2. – C. 283-286.

46. Pavlov D. V. et al. Multi-purpose nanovoid array plasmonic sensor produced by direct laser patterning //Nanomaterials. – 2019. – T. 9. – №. 10. – C. 1348.

47. Hughes T. J. R. The finite element method: linear static and dynamic finite element analysis. – Courier Corporation, 2012.

48. Johson P. B., Christy R. W. Optical constants of transition metals //Phys. Rev. B. – 1974. – T. 9. – C. 5056-5070.

49. Kelly R. L. Program of the 1972 Annual meeting of the optical society of america //JOSA. – 1972. – T. 62. – №. 11. – C. 1336-1336.

50. Klimov V. I. (ed.). Nanocrystal quantum dots. – CRC press, 2017.

51. Sadrieva Z. et al. Multipolar origin of bound states in the continuum //Physical Review B. – 2019. – T. 100. – №. 11. – C. 115303.

52. Wang X. W. et al. Laser-induced translative hydrodynamic mass snapshots: noninvasive characterization and predictive modeling via mapping at nanoscale //Physical Review Applied. – 2017. – T. 8. – №. 4. – C. 044016.